Report

Cell Reports

Stimulation of medial amygdala GABA neurons with kinetically different channelrhodopsins yields opposite behavioral outcomes

Graphical abstract

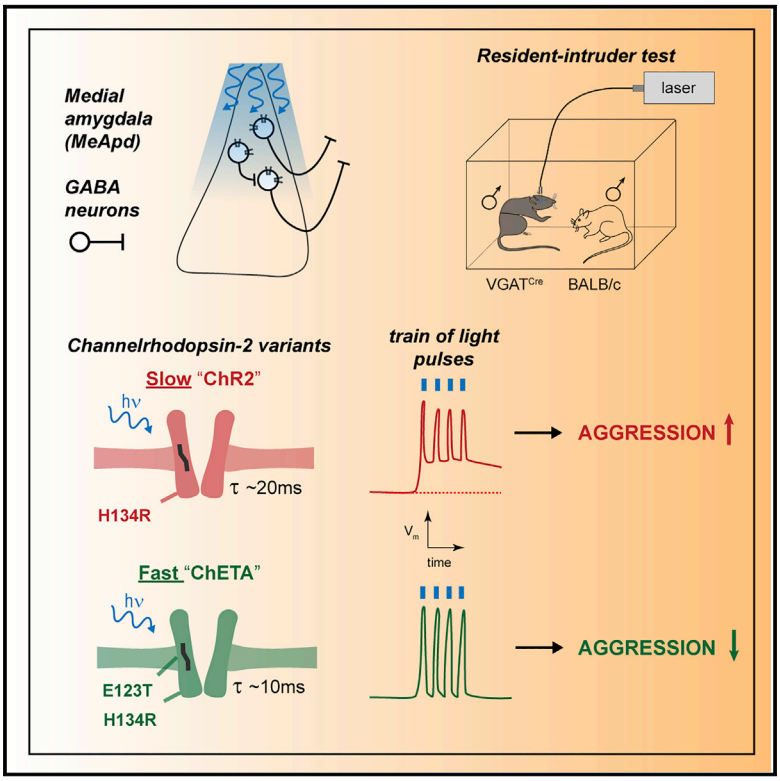

Highlights

- Optogenetic stimulation of MeApd GABA neurons using ChETA reduces aggression
- Stimulation with the slow channelrhodopsin variant ChR2 increases aggression
- Caution is needed when choosing optogenetic tools for *in vivo* experiments
- The role of MeApd GABA neurons in aggression should be further investigated

Authors

Aiste Baleisyte, Ralf Schneggenburger, Olexiy Kochubey

Correspondence

ralf.schneggenburger@epfl.ch (R.S.), olexiy.kochubey@epfl.ch (O.K.)

In brief

MeApd GABA neurons control social behavior including aggression. Baleisyte et al. show that kinetically different channelrhodopsins employed to activate MeApd GABA neurons drive opposite changes of inter-male aggression in mice. The study opens a discussion on which channelrhodopsin variants should be used in future fundamental and translational studies.

Baleisyte et al., 2022, Cell Reports *39*, 110850
May 24, 2022
https://doi.org/10.1016/j.celrep.2022.110850

CellPress

Cell Reports

CellPress
OPEN ACCESS

Report

Stimulation of medial amygdala GABA neurons with kinetically different channelrhodopsins yields opposite behavioral outcomes

Aiste Baleisyte,[1,2] Ralf Schneggenburger,[1,*] and Olexiy Kochubey[1,3,*]

[1]Laboratory of Synaptic Mechanisms, Brain Mind Institute, School of Life Sciences, École Polytechnique Fédérale de Lausanne (EPFL), 1015 Lausanne, Switzerland

[2]Present address: Translational MRI in Neuroscience and Rare Diseases, Roche Pharma Research and Early Development, Roche Innovation Center, F. Hoffmann-La Roche, Ltd., 4070 Basel, Switzerland

[3]Lead contact

*Correspondence: ralf.schneggenburger@epfl.ch (R.S.), olexiy.kochubey@epfl.ch (O.K.)

https://doi.org/10.1016/j.celrep.2022.110850

SUMMARY

The medial amygdala (MeA) receives pheromone information about conspecifics and has crucial functions in social behaviors. A previous study showed that activation of GABA neurons in the postero-dorsal MeA (MeApd) with channelrhodopsin-2^{H134R} (ChR2) stimulates inter-male aggression. When performing these experiments using the faster channelrhodopsin^{H134R,E123T} (ChETA), we find the opposite behavioral outcome. A systematic comparison between the two channelrhodopsin variants reveals that optogenetic activation of MeApd GABA neurons with ChETA suppresses aggression, whereas activation under ChR2 increases aggression. Although the mechanism for this paradoxical difference is not understood, we observe that activation of MeApd GABA neurons with ChR2 causes larger plateau depolarizations, smaller action potentials, and larger local inhibition than with ChETA. Thus, the channelrhodopsin variant used for *in vivo* optogenetic experiments can radically influence the behavioral outcome. Future work should continue to study the role of specific sub-populations of MeApd GABA neurons in aggression control.

INTRODUCTION

Optogenetic methods allow researchers to control the firing of action potentials (APs) in specific neuronal populations by light and to observe the influence of this manipulation on animal behavior (Deisseroth, 2015; Tye and Deisseroth, 2012; Zhang et al., 2007). Channelrhodopsin-2 from *Chlamydomonas reinhardtii* was among the first light-sensitive ion transporters made available for optogenetic studies (Boyden et al., 2005; Nagel et al., 2002, 2005; Sineshchekov et al., 2002). A point mutation was introduced in early work to increase the stationary photocurrent (H134R; Nagel et al., 2005), giving rise to the channelrhodopsin-2^{H134R} variant, called here ChR2. Nevertheless, the off kinetics of ChR2 are quite slow, which can cause large plateau depolarizations in neurons (Berndt et al., 2011; Mattis et al., 2012). Therefore, a faster variant, channelrhodopsin-2$^{H134R,\ E123T}$, called ChETA, was subsequently engineered (Gunaydin et al., 2010). In addition, other light-gated ion channels with fast kinetics have become available, like Chronos and ChIEF (Klapoetke et al., 2014; Lin et al., 2009). Nevertheless, the slower ChR2 remains a popular tool for *in vivo* optogenetics, maybe because fundamentally different behavioral outcomes between kinetically different channelrhodopsins have so far not been found.

The medial amygdala (MeA) plays a crucial role in social behaviors (Anderson, 2012; Haller, 2018; Lischinsky and Lin, 2020; Raam and Hong, 2021). Its postero-dorsal division (MeApd) contains a large number of GABA neurons, many of which are long-range projection neurons (Bian et al., 2008; Canteras et al., 1995; Choi et al., 2005; Keshavarzi et al., 2014). Early lesion studies and recent optogenetic and chemogenetic studies showed a role of the MeA in aggression control (Chen et al., 2019; Hong et al., 2014; Miczek et al., 1974; Miller et al., 2019; Nordman and Li, 2020; Padilla et al., 2016; Unger et al., 2015; Vochteloo and Koolhaas, 1987; see review by Haller, 2018). Particularly, using a *VGAT-^{Cre}* mouse line, it was shown that optogenetic activation of MeApd GABA neurons with ChR2 led to a marked increase of attacks in the resident-intruder test (Hong et al., 2014). This gave rise to the generally accepted view that the activity of MeApd GABA neurons is sufficient to drive aggression (see reviews by Aleyasin et al., 2018; Chen and Hong, 2018; Hashikawa et al., 2016; Lischinsky and Lin, 2020).

Here, we report that using ChR2 and ChETA for optogenetic stimulation of MeApd-GABA neurons gives rise to paradoxical opposite behavioral outcomes in studies of inter-male aggression. Our study shows that channelrhodopsin variants have to be selected and validated with care for *in vivo* experiments. Furthermore, the role of specific MeApd GABA neuron sub-populations in aggression control should be further investigated.

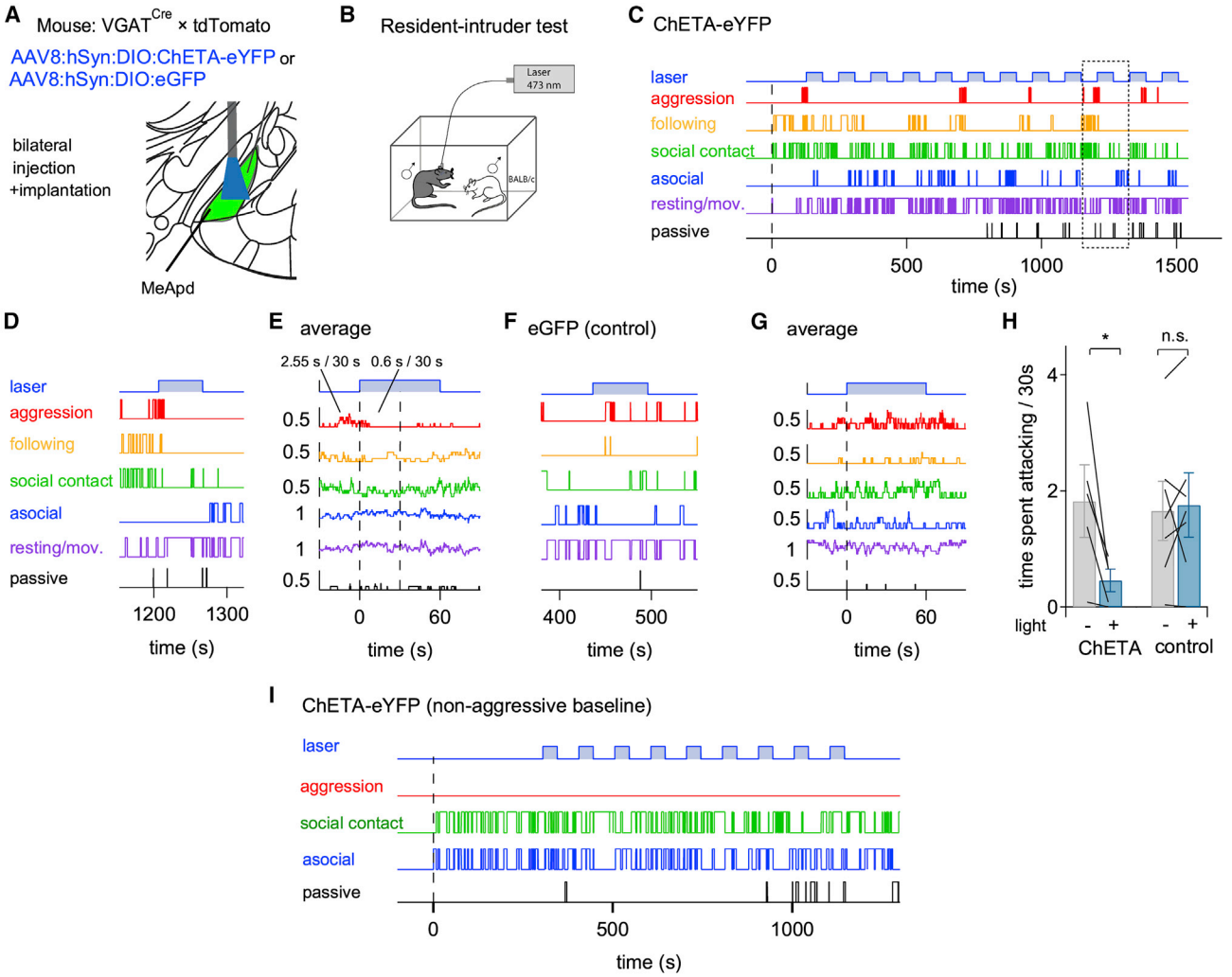

Figure 1. *In vivo* optogenetic stimulation of MeApd GABA neurons using ChETA inhibits inter-male aggression

(A) Schematic of the experimental approach.

(B) Schematic of a resident-intruder test with *in vivo* optogenetics.

(C) Behavior of a resident mouse quantified during a resident-intruder test (see STAR Methods). 60-s long trains of 473 nm laser light pulses (5 ms, 20 Hz rate, 10 mW) were interleaved by 60 s dark periods. An intruder was introduced at t = 0.

(D) An example light-train episode (dotted box in C).

(E) Light-onset-aligned behavior traces averaged over n = 12 repeats in an example mouse. The average times the mouse spent attacking in a 30 s interval before and after the train onset are indicated. Data in (C)–(E) are from the same example animal.

(F and G) As in (D) and (E) but from a mouse expressing eGFP.

(H) Quantifications of time spent attacking before or during the first 30 s of the light train from n = 5 and 7 mice expressing ChETA or EGFP, respectively. Two-tailed unpaired t test was performed. *p < 0.05; n.s., non-significant.

(I) An example mouse that did not show baseline aggression and in which optogenetic stimulation with ChETA did not trigger aggression. Similar observations were made in n = 3 non-aggressive mice.

Data are represented as mean ± SEM. See also Figure S1.

RESULTS

Optogenetic activation of MeApd GABA neurons with ChETA suppresses aggression

Our original aim was to investigate the role of molecularly defined subtypes of MeApd GABA neurons in aggression control. We first wished to reproduce the earlier finding that optogenetic stimulation of MeApd GABA neurons, using VGAT^{Cre} mice, leads to an increase of aggression (Hong et al., 2014). We bilaterally injected an AAV8 vector (AAV8:hsyn:DIO:ChETA-eYFP) into the MeApd of *VGAT^{Cre} x tdTomato* mice to drive the Cre-dependent expression of ChETA and implanted optic fibers above the injection sites (Figure 1A; see STAR Methods). Control mice received a homologous AAV8 vector driving the Cre-dependent expression of eGFP (see key resources table). Four weeks later, MeApd GABA neurons were activated optogenetically during a resident-intruder test,

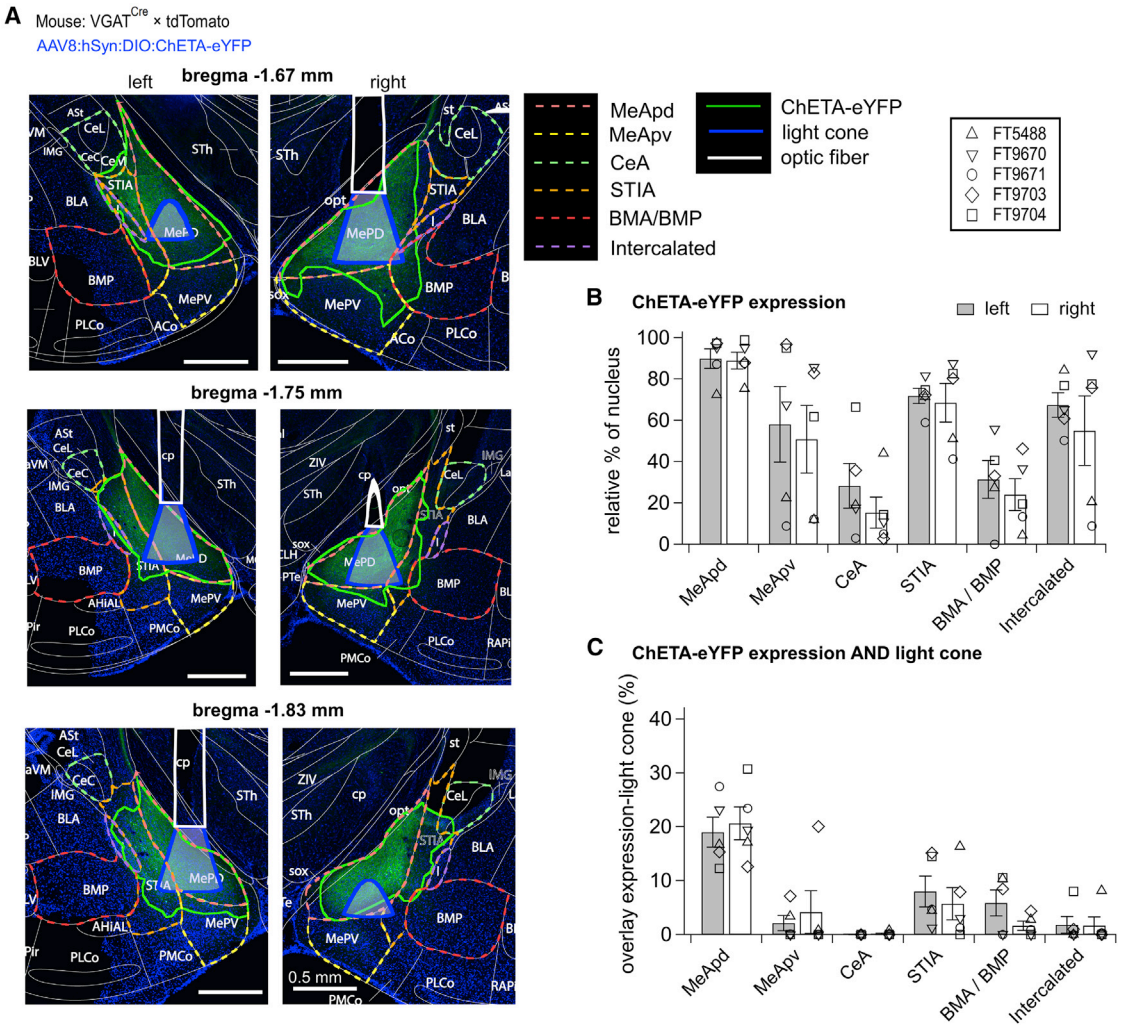

Figure 2. Histological analysis confirms targeting of the MeApd for optogenetic stimulation

(A) Fluorescent images of coronal brain sections at the level of the MeApd (bregma levels indicated), obtained post hoc from a ChETA-expressing mouse. Shown are regions of ChETA-eYFP expression (green channel), which were manually outlined (solid green lines); the reconstructed cross-sections of the optic fibers (solid white lines); the outlines of brain areas according to Franklin and Paxinos (2013) (dashed lines). Scale bars, 500 μm.

(B) Fraction of each brain area expressing ChETA-eYFP, analyzed for n = 5 ChETA-expressing mice shown in Figure 1. MeApv, postero-ventral MeA; CeA, central amygdala; BMA/BMP, basomedial anterior/posterior amygdalae; STIA, intraamygdaloid bed nucleus of stria terminals.

(C) Fraction of each brain area that expressed ChETA-eYFP and overlapped with the light cone for the same n = 5 mice as in (B).

Data are represented as mean ± SEM.

using BALB/cByJ males as intruders (Figure 1B). We used trains of blue-light pulses (5 ms, 10 mW, 20 Hz, length of 30 or 60 s) delivered at regular intervals (60 s dark periods) to avoid a possible bias by experimenter-driven stimulation.

Surprisingly, we found that aggression occurred mostly in the absence of light stimulation and that light stimulation often stopped attacks in ChETA-expressing mice (Figures 1C and 1D). The average behavioral scores aligned to the onset of optogenetic stimulation showed a reduced attack activity during the light as compared with the preceding dark periods (0.6 s spent attacking during 30 s versus 2.55 per 30 s; Figure 1E). Such a reduced aggression was found in all mice from the ChETA group but not in eGFP-expressing control mice (Figure 1H; $p = 0.0385$, $n = 5$; and $p = 0.73$, $n = 7$ mice, respectively; two-tailed paired t test). Importantly, in an additional three mice that showed no spontaneous aggression, optogenetic activation of MeApd GABA neurons did not trigger attacks (Figure 1I). Furthermore, in $n = 2$ VGAT^{Cre} mice expressing ChETA, we observed that the suppression of aggression depended on the light intensity of optogenetic stimulation (Figure S1). Together, these findings suggest that optogenetic activation of MeApd GABA neurons inhibits aggression (Figures 1 and S1), opposite to the previous results (Hong et al., 2014).

We next verified if the MeApd was well targeted for optogenetic stimulation by reconstructing the expression of ChETA-eYFP and the fiber placements (Figure 2). We found that

90% ± 5% and 89% ± 4% of the cumulative area of the MeApd expressed ChETA-eYFP (Figures 2A and 2B; n = 5 mice). The expression of ChETA also extended into the neighboring subnuclei of the amygdala, albeit covering lower area fractions (Figures 2A and 2B). Next, based on the optic fiber tip positions, we estimated the fractions of the brain areas that expressed ChETA and were likely exposed to light (Aravanis et al., 2007; STAR Methods). The largest overlap between ChETA expression and the illuminated areas was found for the left and right MeApd (19.0% ± 2.8% and 20.7% ± 3.1%; Figure 2C). Among the other areas, the bed nucleus of the stria terminalis, intraamygdaloid part (STIA) had a somewhat larger fractional overlap (8.0% ± 2.9% and 5.7% ± 3.0% for the left and right sides; Figure 2C). However, a large part of ChETA-eYFP fluorescence in this structure probably represents axons projecting out of the MeApd. Thus, the MeApd was well targeted in our optogenetic activation experiments.

Optogenetic activation of MeApd GABA neurons with ChR2 stimulates aggression

We next sought to identify the factors underlying the difference between our results (Figure 1) and the previous study, which used an AAV2 vector to express the slower channelrhodopsin variant ChR2 (Hong et al., 2014). Therefore, we next employed ChR2 in an AAV2 serotype vector (AAV2:EF1α:DIO:ChR2-eYFP; Figure 3A; see key resources table), as close as possible to the previously used custom construct. With this vector, optogenetic activation of MeApd GABA neurons stimulated aggression. In an example mouse (Figures 3B and 3C), the attack activity increased during the light periods compared with the periods before light (4.86 versus 0.22 s per 30 s; Figure 3D). Across all mice expressing AAV2:ChR2, optogenetic stimulation significantly increased aggression (Figure 3G; p = 0.012, two-tailed paired t test, n = 7 mice). On the other hand, in control mice expressing eYFP under an AAV2 vector (AAV2:EF1α:DIO:eYFP), stimulation with blue light did not increase aggression (Figure 3G; p = 0.35, two-tailed paired t test, n = 3 mice). Furthermore, in a ChR2-expressing mouse that showed no spontaneous aggression, the light trains triggered time-locked attacks (Figure 3H). A post hoc histological analysis showed that the MeApd was well targeted for optogenetic stimulation (Figure S2).

These experiments suggest that optogenetic stimulation of the MeApd GABA neurons using ChETA versus ChR2 lead to an opposite modulation of aggressive behavior (compare Figures 1 and 3A–3H). However, viral vectors of different serotypes (AAV8 and AAV2) were used in the above experiments. We therefore next performed experiments with the two remaining combinations of AAV serotypes and channelrhodopsin variants. This showed that expressing ChETA with an AAV2 vector resulted in a significant decrease in aggression during stimulation with light (Figures 3I–3K and 3O, p = 0.0039, n = 9 mice; Wilcoxon two-tailed test). Conversely, when ChR2 was expressed with an AAV8 vector, light stimulation led to an increase of aggression (Figures 3L–3O, p = 0.0391, n = 8 mice; Wilcoxon two-tailed test). In control mice expressing either eYFP using an AAV2 vector or else eGFP using AAV8, light application did not modulate aggression (Figure 3O; p = 0.41, n = 11, two-tailed Wilcoxon test, and p = 0.53, n = 7 mice, two-tailed paired t test, respectively). These experiments show that it is the channelrhodopsin variant (ChR2 versus ChETA), but not the AAV serotype, that determines the behavioral outcome after optogenetic activation of MeApd GABA neurons.

We wished to investigate the sub-populations of MeApd GABA neurons that were transduced by the AAV2 and AAV8 vectors. For this, we injected a mix of an AAV2 and an AAV8 vector into the MeApd of VGAT^{Cre} mice to drive the expression of eYFP and tdTomato, respectively (Figures S3A–S3I; see supplemental information for details on the AAV constructs). We found that the AAV2 vector infected a larger number of MeApd GABA neurons, whereas expression driven by the co-injected AAV8 vector was, in essence, restricted to a sub-population of the AAV2-transfected neurons (Figures S3A–S3I; n = 3 mice). This finding was different from previous findings in cortical neurons, in which the transduction efficiency of AAV8 was higher than that of AAV2 (Aschauer et al., 2013; Watakabe et al., 2015). Although AAV2 transfected a larger number of MeApd GABA neurons than AAV8, the optogenetic experiments did not reveal a strong qualitative difference between these serotypes, given that the same channelrhodopsin variant was used (Figure 3O). Thus, we conclude that the AAV serotype was not a key factor for the different behavioral outcomes.

ChETA and ChR2 are distinguished by a single point mutation (see introduction), and it is unlikely that this difference should cause a differential expression between subtypes of MeApd GABA neurons. Nevertheless, to investigate this possibility, we co-injected equal amounts of AAV2 vectors driving the Cre-dependent expression of ChETA (AAV2:EF1α:DIO:ChETA-eYFP; see above) and of ChR2 (AAV2:EF1α:DIO:ChR2-mCherry; see key resources table) into the MeApd of VGAT^{Cre} mice (Figures S3J–S3P). We found that a majority of cells co-expressed both variants (78% ± 3.9%; n = 4 mice), while smaller percentages of neurons expressed only one of the variants (ChR2: 8.1% ± 1.1%; ChETA: 13.7% ± 3.0%, n = 4 mice; Figures S3O and S3P). We assume that these small neuronal sub-populations expressing a single construct arise stochastically due to the uptake of only one type of viral vector per neuron. These results thus suggest that ChETA and ChR2 target MeApd GABA neurons largely non-selectively and that a large population of MeApd GABA neurons can equally well express each channelrhodopsin variant.

In the behavioral experiments, we noticed that the attack activity in the dark periods was significantly lower in mice expressing ChR2 than in mice expressing ChETA (Figure 3O, gray bars and Figure 3P, $p < 10^{-4}$, Mann-Whitney test; n = 15 and n = 14 mice, respectively). This can be explained by considering that under ChR2, aggressive behaviors take place preferentially during the light periods (Figures 3A–3H, 3L, and 3M), which might "deplete" the amount of aggression in the absence of light. Conversely, with ChETA, light application suppresses aggression (Figures 1 and 3I–3K), and therefore, aggression bouts occur preferentially in the absence of light. To validate this view and to exclude the possibility that expression of the two channelrhodopsin variants leads to genuine changes in the baseline aggression, we analyzed the baseline aggression during ~5 min of each experiment, in between the admission of the intruder mouse and the application of the first light trains.

CellPress
OPEN ACCESS

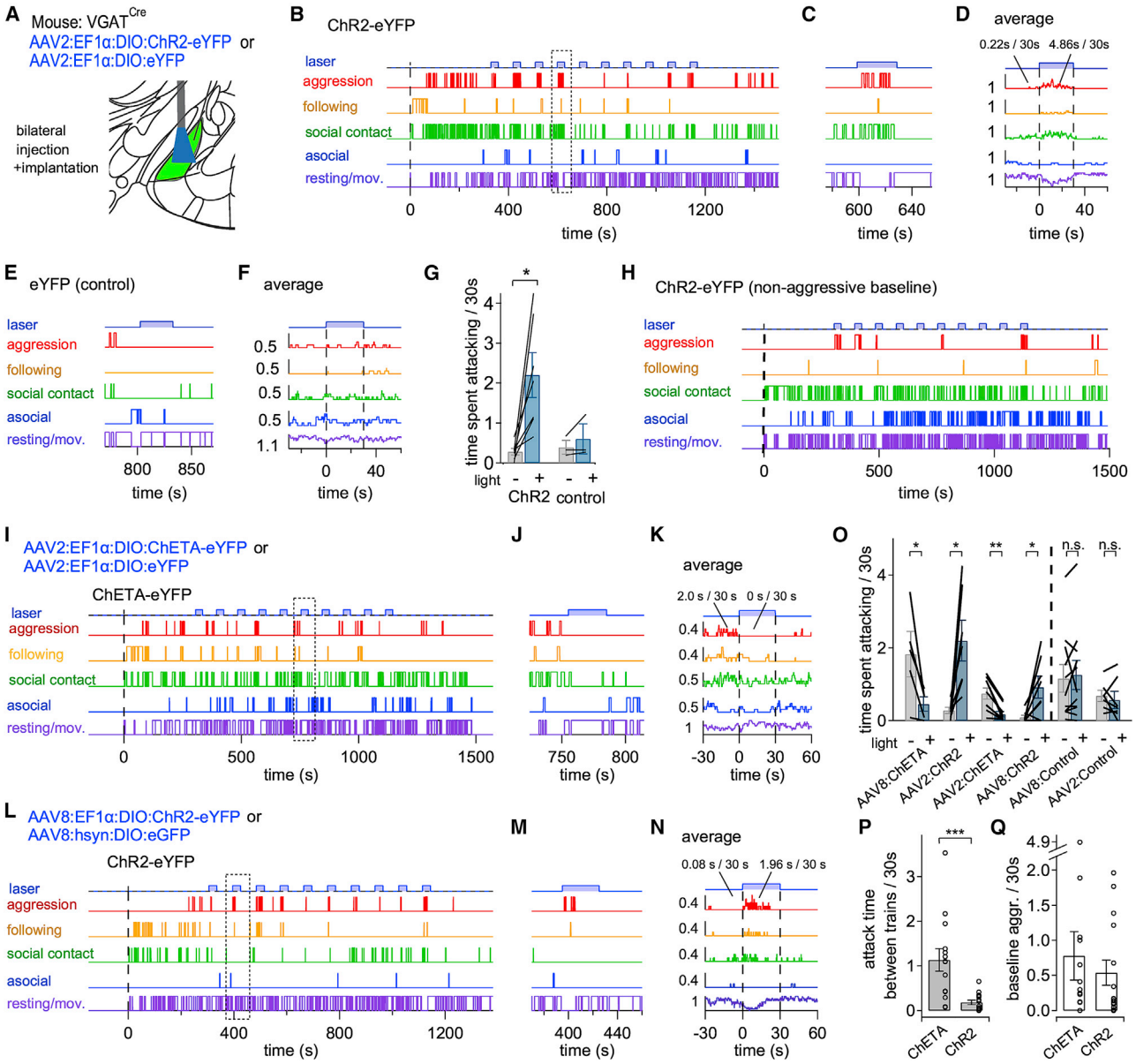

Figure 3. *In vivo* optogenetic activation of MeApd GABA neurons using ChETA or ChR2 leads to opposite modulation of aggressive behavior

(A) Schematic of the experimental approach.

(B) Behavior of an example mouse expressing ChR2 in MeApd GABA neurons during the resident-intruder test with optogenetic stimulation.

(C and D) Example light-train episode (C; dotted box in B), and average light-onset-aligned behavior traces (D; n = 10 trains) for the same mouse as in (B). Note the increase of aggression during the light train.

(E and F) Behavior data for a mouse expressing eYFP (control group).

(G) Quantification of time spent attacking in 30 s intervals before and during the light train in mice expressing ChR2 (n = 7) or eYFP (n = 3). Note the stimulation of aggression in the ChR2 group.

(H) An example mouse of the ChR2 group in which no baseline aggression occurred. Note that light trains induce marked attack behavior.

(I–K) Behavior of an example mouse expressing ChETA using an AAV2 vector. Note the suppression of aggression during the light (K; average of n = 10 trains).

(L–N) Behavior of an example mouse expressing ChR2 using an AAV8 vector. Note the increased aggression during the light (N; average of n = 10 trains).

(O) Quantification of time spent attacking in a 30 s interval before (gray bars) or during the light-train stimulation (blue bars) for all tested conditions. The two left-most datasets re-plot the data from Figures 1H and 3G. The third and the fourth datasets show the data with AAV2:ChETA (n = 9 mice) and with AAV8:ChR2 (n = 8 mice). The two right-most datasets show the data with AAV8:eGFP and AAV2:eYFP (control groups). Two-tailed Wilcoxon or paired t tests were performed. *p < 0.05; **p < 0.01; n.s., non-significant.

(P and Q) Time spent attacking per 30 s period in between the light stimulation trains (P; pooled from the gray bars in O) or during the ~5 min baseline before the first optogenetic train (Q), for mice expressing ChETA or ChR2. Two-tailed Mann-Whitney test was performed. ***p < 0.001.

Data are represented as mean ± SEM. See also Figures S2 and S3.

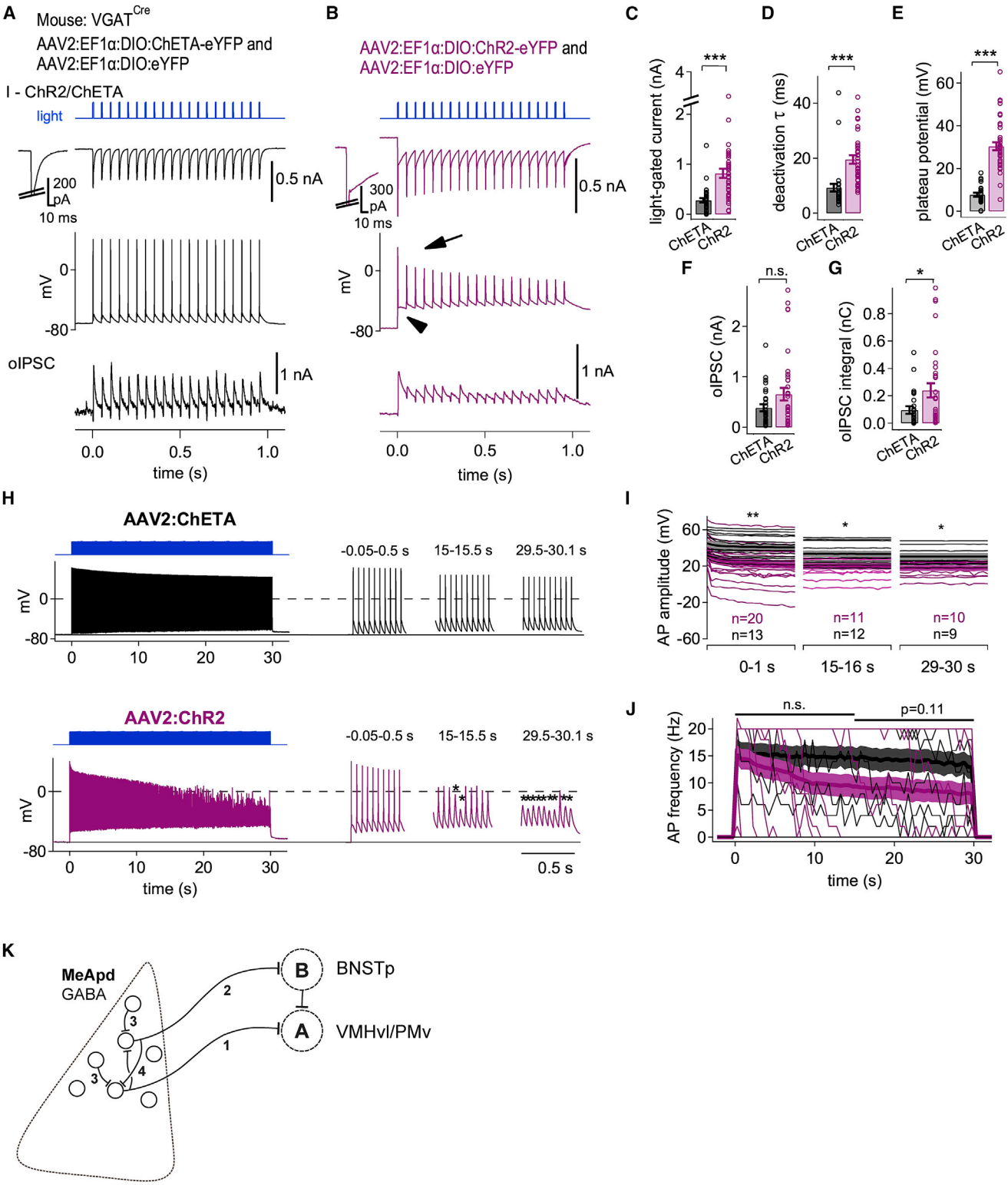

Figure 4. Optogenetic stimulation with ChR2 causes plateau depolarizations, AP amplitude decrements and failures, and stronger local inhibition of MeApd GABA neurons

(A and B) Example whole-cell recordings from the MeApd GABA neurons expressing ChETA (A) or ChR2 (B) in response to short (1 s) trains of blue light pulses (λ = 470 nm, 5 ms at 20 Hz; blue traces). Traces from top to bottom: light-gated currents recorded at -70 mV (insets show the first pulse response; unclamped Na^+ current was clipped); membrane potential response; oIPSCs recorded at 0 mV.

(legend continued on next page)

This baseline aggression was indistinguishable between mice expressing ChETA and ChR2 (Figure 3Q, p = 0.75, Mann-Whitney test; n = 14 and n = 15 mice). Thus, the baseline level of aggression is not influenced by the expression of ChETA versus ChR2 in MeApd GABA neurons, and furthermore, the dark intervals in between the regular trains of blue-light stimulation cannot be used to define a true baseline level of aggression.

Taken together, the experiments in Figure 3 showed that two closely related channelrhodopsin variants, ChETA and ChR2, produce opposite behavioral outcomes when used for optogenetic stimulation of MeApd GABA neurons.

ChR2 causes large plateau depolarizations, AP amplitude decrements, and increased local inhibition of MeApd GABA neurons

In the search for a possible mechanism underlying the opposite behavioral outcomes of the *in vivo* optogenetic experiments with ChETA and ChR2, we compared the responses to blue-light pulses of MeApd GABA neurons expressing each channelrhodopsin variant. ChR2, or ChETA, was expressed in a Cre-dependent manner using the same AAV2 serotype vectors as used in the behavioral experiments; in addition, cytosolic eYFP was expressed from a co-injected AAV2 vector to enable the visualization of transfected neurons in slices (see STAR Methods).

We first recorded the responses of MeApd GABA neurons to 1 s trains of blue light (5 ms pulses at 20 Hz) under voltage clamp (Figures 4A and 4B, top). Light-activated currents had larger amplitudes and slower deactivation kinetics with ChR2 than with ChETA (Figure 4C, $p < 10^{-4}$, n = 31 and n = 35 cells, and Figure 4D, $p < 10^{-4}$, n = 30 and n = 33 cells for ChR2 and ChETA, respectively; two-tailed Mann-Whitney test; see also Berndt et al., 2011; Gunaydin et al., 2010; Mattis et al., 2012). In current-clamp recordings, we found that the 1 s light trains reliably triggered APs in both ChETA- and ChR2-expressing neurons (Figures 4A and 4B, middle) except in a few neurons in which the light-activated currents were small (<60 pA; Figure S4A). A difference between the channelrhodopsin variants was a prominent plateau depolarization in ChR2-expressing neurons (Figure 4B, middle, arrowhead), which was significantly larger than in ChETA-expressing neurons (30.4 ± 1.9 versus 7.7 ± 0.9 mV; Figure 4E; $p < 10^{-4}$, n = 28 and n = 25 cells; two-tailed t test). One consequence of the plateau potential was a rapid decrease of the AP amplitude in ChR2-expressing neurons presumably caused by inactivation of voltage-gated Na^+ channels (Figure 4B, middle, arrow). As a consequence, the average AP amplitudes for the 1 s light train were significantly smaller with ChR2 than with ChETA (20.2 ± 3.5 and 35.2 ± 3.5 mV; p < 0.0043; two-tailed t test).

We next recorded optogenetically evoked inhibitory postsynaptic currents (oIPSCs) at a holding potential close to the reversal of the ChR2/ChETA currents (0 mV; Figures 4A and 4B, bottom). While the first oIPSC amplitudes were not different between the two groups (Figure 4F; p = 0.141, n = 30 and n = 34 ChR2 and ChETA cells; two-tailed Mann-Whitney test), the synaptic charge transfer during the 1 s trains was significantly larger in the ChR2 group than in the ChETA group (Figure 4G; p = 0.012, n = 30 and 35, respectively; two-tailed Mann-Whitney test). This difference might contribute to the opposite behavioral outcomes between ChETA and ChR2 (see discussion).

In a subset of recorded cells, we applied light trains of the same duration as the ones used *in vivo* (30 s long trains; 5 ms pulse width, 20 Hz repetition; Figure 4H). As for the 1 s long trains, we found a larger plateau depolarization with ChR2 than with ChETA, both early (0–1 s: 30.4 ± 2.3 versus 10.2 ± 1.1 mV; $p < 10^{-4}$) and late during the train (20–30 s: 37.5 ± 2.1 versus 11.2 ± 1.2 mV; $p < 10^{-4}$; n = 24 and 17 recordings; two-way repeated measures (RM)-ANOVA for the channelrhodopsin variant, followed by Šídák's multiple comparisons test). As in the short trains, the AP amplitudes decreased more strongly with ChR2 than with ChETA upon repeated stimuli (Figure 4I; for the time intervals 0–1 s: p = 0.0096; 15–16 s: p = 0.011; 29–30 s: p = 0.0113; two-way RM-ANOVA for the channelrhodopsin variant). With ChR2, we often observed AP failures especially in the second half of the trains (Figure 4H, star symbols). This resulted in a reduction of the effective AP frequency during the last half of the 30 s train (Figure 4J); however, the difference of the frequency attained with ChETA did not reach statistical significance (p = 0.11, n = 25 and n = 18, two-tailed Mann-Whitney test).

Finally, we investigated whether ChETA and ChR2 had a differential capacity to drive APs in distinct sub-populations of MeApd GABA neurons. For this, we classified the recorded neurons into six types based on their intrinsic AP-firing properties (Figures S4B and S4C; STAR Methods). We found some heterogeneity across neuron firing types in their ability to follow optogenetic stimuli (Figure S4D). However, the dataset was not sufficiently complete to test for differences in AP-following across the six functional neuron types.

DISCUSSION

The MeApd plays a crucial role in the control of social behaviors; interestingly, this brain area contains a mix of GABAergic

(C–G) Quantifications of light-gated current amplitudes (C), decay time constant τ (D), plateau depolarization (E), oIPSC amplitude (F), and oIPSC integral (G), each for ChR2-and ChETA-expressing MeApd GABA neurons (gray and pink bars, respectively). Data are represented as mean ± SEM. Two-tailed Mann-Whitney or t tests were performed. *p < 0.05; ***p < 0.001; n.s., non-significant.

(H) Examples of AP firing induced by long trains (30 s, 5 ms pulses at 20 Hz), both under ChETA (top) or ChR2 (bottom). Insets show 0.5 s long stretches at the indicated times.

(I) Peak AP amplitudes during three time intervals of the long trains. Note that only cells with no AP failures during each interval were included, which causes a decreased number of individual traces (thin lines); average traces are shown with thicker lines. Two-way RM-ANOVA was performed. *p < 0.05; **p < 0.01.

(J) Plot of effective AP frequency attained by 20 Hz light-train stimulation in ChETA- or ChR2-expressing neurons (bin width 0.5s). Individual traces (thin lines) and the average traces for each group are shown. Color shadings represent ± SEM around mean traces. Two-tailed Mann-Whitney tests were performed. n.s., non-significant.

(K) Scheme of MeApd GABA neurons and their possible output connections.

See discussion. See also Figure S4.

projection neurons, local inhibitory interneurons, and glutamatergic neurons (Bian, 2013; Choi et al., 2005; Keshavarzi et al., 2014). Previous work showed that optogenetic activation of the entire population of MeApd GABA neurons with the slow channelrhodopsin variant, ChR2, stimulated inter-male aggression (Hong et al., 2014). Surprisingly, we found that optogenetic activation of MeApd GABA neurons with ChETA, using the same VGAT^{Cre} mouse line as employed previously, caused the opposite behavioral outcome, i.e., an inhibition of aggression. This prompted us to perform a side-by-side comparison of the two channelrhodopsin variants, each expressed by two AAV vectors. These experiments unambiguously showed that activation of MeApd GABA neurons with ChETA reduced aggression, whereas activation with ChR2 increased aggression, independent of the AAV serotype used to express the channelrhodopsins (Figures 1 and 3). Thus, paradoxically, stimulation of GABA neurons in a defined brain area, using two kinetically different channelrhodopsins, produces opposite behavioral outcomes.

What is the underlying mechanism of this paradoxical finding? In the search for an explanation, it should be considered that MeApd GABA neurons are a heterogeneous population of neurons that differ molecularly (Wu et al., 2017), by their AP-firing patterns (Figure S4), and by the identity of their local- and long-range projection targets (Bian, 2013; Keshavarzi et al., 2014; see Figure 4K). First, there is anatomical evidence for a projection of MeApd GABA neurons to hypothalamic targets like the VMH and the PMv (Canteras et al., 1995; Choi et al., 2005; Lo et al., 2019; Figure 4K, pathway 1). Because neurons in the ventromedial hypothalamic (VMH) and premammilary ventral (PMv) nuclei drive aggression (Chen et al., 2020; Lee et al., 2014; Lin et al., 2011; Stagkourakis et al., 2018), an inhibitory pathway from the MeApd to these hypothalamic neurons is expected to suppress aggression, although such a mechanism would need to be demonstrated directly in future work. Second, although Hong et al. (2014) did not identify the downstream target(s) of the MeApd responsible for their observed effects, they postulated a disinhibitory pathway reaching hypothalamic targets to explain their results. Consistent with this notion, it was shown subsequently that MeA GABA neurons expressing D1R or NPYR1 can stimulate aggression via a projection to the bed nucleus of the stria terminalis principal nucleus (BNSTp), in what might present one limb of a disinhibitory pathway to the hypothalamus (Figure 4K, pathway 2; see Miller et al., 2019; Padilla et al., 2016; note, however, that D1R+ and NPYR1+ neurons are localized somewhat more ventrally in the MeA and may contain a certain fraction of non-GABA neurons). In addition to these and other possible long-range output pathways, there are local inhibitory connections in the MeApd, likely both from inhibitory interneurons (Figure 4K, pathway 3), and from axonal collaterals of projection neurons (Figure 4K, pathway 4), onto the long-range projecting MeApd GABA neurons. This circuit model for MeApd GABA neurons is speculative at present but can provide a conceptual framework for the discussion, and for future studies on the roles of specific MeApd GABA neurons in controlling aggression.

Our *ex vivo* electrophysiology experiments have shown large plateau potentials when MeApd GABA neurons were stimulated under ChR2 (Figure 4; Berndt et al., 2011; Gunaydin et al., 2010; Mattis et al., 2012). Such plateau depolarizations were previously shown to cause a depolarization-induced block of AP firing in certain interneurons (Herman et al., 2014), and in cortex, ChR2 was shown to cause differential temporal activation patterns compared with faster channelrhodopsin variants (Jun and Cardin, 2020). Here, the plateau depolarizations under ChR2 caused a somewhat higher AP failure rate during the second half of the stimulation trains (Figure 4J); a difference that could contribute to the opposite behavioral outcomes. However, the time courses of attack behavior show that the difference in behavioral outcomes is already present in the first half of the 30 s light trains (see Figures 1E and 3K for ChETA and Figures 3D and 3N for ChR2; see also Hong et al., 2014 and their Figure 2). Therefore, it seems more likely that under each channelrhodopsin variant, sub-populations of MeApd GABA neurons that finally lead to a stimulation—or else a suppression—of aggression are already activated more efficiently a few seconds after the start of optogenetic activation. In this respect, the observation of larger oIPSC integrals with ChR2 as compared with ChETA might be relevant (Figure 4G). Larger integrals of oIPSCs with ChR2 are likely caused by passive propagation of the plateau depolarizations to the local (but maybe not to the distant) nerve terminals, where these unphysiologically long depolarizations might cause increased asynchronous GABA release (Alle and Geiger, 2006; Awatramani et al., 2005). If one assumes that the increased local inhibition preferentially acts on GABAergic projection neurons to the VMH (Figure 4K, pathway 1), then this mechanism would lead to a disinhibition of VMH neurons, thus stimulating aggression. Furthermore, it is possible that ChETA and ChR2 recruit AP firing of functionally different MeApd GABA neurons with different efficiencies. We found six AP-firing types of MeApd GABA neurons (Figure S4; see also Keshavarzi et al., 2014 for the MeApv); however, our electrophysiological dataset was not sufficiently large to test this possibility. Lastly, although we showed that ChR2 and ChETA can be expressed simultaneously by a large subpopulation of MeApd GABA neurons (Figures S3J–S3P), it remains possible that a differential expression of ChR2 versus ChETA, even if only in two small sub-populations of MeApd GABA neurons, could tip the net behavioral outcome from stimulation to suppression of aggression. In summary, we currently cannot identify the mechanism that underlies the differential behavioral outcome, but we think the reason must lie in a functional heterogeneity between subpopulations of MeApd GABA neurons.

Considering the paradoxical opposite behavioral effects we observed here after optogenetic activation of inhibitory neurons, channelrhodopsin variants should be carefully selected in future studies. Ideally, it should be tested *in vivo* whether optogenetic activation with a given channelrhodopsin variant leads to the expected increase in AP firing of the desired neuron population. In general, we would recommend to discontinue the use of slower forms of channelrhodopsin in future work because these are more prone to artifacts like plateau depolarizations and decrements of AP amplitudes (Figure 4; Berndt et al., 2011; Herman et al., 2014; Jun and Cardin, 2020; Mattis et al., 2012). Especially for a desired activation of long-range GABA projection neurons, plateau depolarizations might lead to complex artifacts when the slow ChR2 is expressed both in local and long-range inhibitory neurons (see discussion). Furthermore, since optogenetic

activation experiments do not allow us to conclude with certainty whether activity of MeApd GABA neurons stimulates, or else suppresses aggression, the role of this important GABA neuron system in aggression control should be further investigated, with an emphasis on a possible heterogeneity of MeApd GABA neurons.

Limitations of the study

Despite reporting a robust phenomenon, our study did not provide a mechanistic explanation for the opposite behavioral outcome after optogenetic stimulation with ChETA versus ChR2.

STAR★METHODS

Detailed methods are provided in the online version of this paper and include the following:

- KEY RESOURCES TABLE
- RESOURCE AVAILABILITY
  - Lead contact
  - Materials availability
  - Data and code availability
- EXPERIMENTAL MODEL AND SUBJECT DETAILS
- METHOD DETAILS
  - Viral vectors
  - Stereotactic surgery procedures
  - Behavioral testing
  - Histology
  - Image acquisition
  - Patch-clamp electrophysiology
- QUANTIFICATION AND STATISTICAL ANALYSIS
  - Analysis of behavior data
  - Analysis of illuminated brain areas
  - Analysis of expression patterns in the MeA
  - Electrophysiological data analysis
  - Statistical data analysis

SUPPLEMENTAL INFORMATION

Supplemental information can be found online at https://doi.org/10.1016/j.celrep.2022.110850.

ACKNOWLEDGMENTS

We would like to thank Drs. Dayu Lin and Julieta Lischinsky (New York University) for sharing unpublished results and Dr. Bernard Schneider (EPFL) for custom packaging of AAV vectors. Fluorescent microscopy was performed at the Bioimaging and Optics Core Facility (BIOP) at EPFL. This work was supported by the Swiss National Science Foundation, "NCCR Synapsy: The Synaptic bases of mental diseases," project #28 to R.S.

AUTHOR CONTRIBUTIONS

A.B. and O.K. performed the experiments and analyzed the data; O.K., R.S., and A.B. conceived the study and wrote the manuscript.

DECLARATION OF INTERESTS

The authors declare no competing interests.

Received: September 13, 2021
Revised: December 20, 2021
Accepted: April 30, 2022
Published: May 24, 2022

REFERENCES

Aleyasin, H., Flanigan, M.E., and Russo, S.J. (2018). Neurocircuitry of aggression and aggression seeking behavior: nose poking into brain circuitry controlling aggression. Curr. Opin. Neurobiol. *49*, 184–191. https://doi.org/10.1016/j.conb.2018.02.013.

Alle, H., and Geiger, J.R.P. (2006). Combined analog and action potential coding in hippocampal mossy fibers. Science *311*, 1290–1293. https://doi.org/10.1126/science.1119055.

Anderson, D.J. (2012). Optogenetics, sex, and violence in the brain: implications for psychiatry. Biol. Psychiatry *71*, 1081–1089. https://doi.org/10.1016/j.biopsych.2011.11.012.

Aravanis, A.M., Wang, L.P., Zhang, F., Meltzer, L.A., Mogri, M.Z., Schneider, M.B., and Deisseroth, K. (2007). An optical neural interface: in vivo control of rodent motor cortex with integrated fiberoptic and optogenetic technology. J. Neural Eng. *4*, S143–S156. https://doi.org/10.1088/1741-2560/4/3/S02.

Aschauer, D.F., Kreuz, S., and Rumpel, S. (2013). Analysis of transduction efficiency, tropism and axonal transport of AAV serotypes 1, 2, 5, 6, 8 and 9 in the mouse brain. PLoS One *8*, e76310. https://doi.org/10.1371/journal.pone.0076310.

Awatramani, G.B., Price, G.D., and Trussell, L.O. (2005). Modulation of transmitter release by presynaptic resting potential and background calcium levels. Neuron *48*, 109–121. https://doi.org/10.1016/j.neuron.2005.08.038.

Berndt, A., Schoenenberger, P., Mattis, J., Tye, K.M., Deisseroth, K., Hegemann, P., and Oertner, T.G. (2011). High-efficiency channelrhodopsins for fast neuronal stimulation at low light levels. Proc. Natl. Acad. Sci. U S A *108*, 7595–7600. https://doi.org/10.1073/pnas.1017210108.

Bian, X. (2013). Physiological and morphological characterization of GABAergic neurons in the medial amygdala. Brain Res. *1509*, 8–19. https://doi.org/10.1016/j.brainres.2013.03.012.

Bian, X., Yanagawa, Y., Chen, W.R., and Luo, M. (2008). Cortical-like functional organization of the pheromone-processing circuits in the medial amygdala. J. Neurophysiol. *99*, 77–86. https://doi.org/10.1152/jn.00902.2007.

Boyden, E.S., Zhang, F., Bamberg, E., Nagel, G., and Deisseroth, K. (2005). Millisecond-timescale, genetically targeted optical control of neural activity. Nat. Neurosci. *8*, 1263–1268. https://doi.org/10.1038/nn1525.

Canteras, N.S., Simerly, R.B., and Swanson, L.W. (1995). Organization of projections from the medial nucleus of the amygdala: a PHAL study in the rat. J. Comp. Neurol. *360*, 213–245. https://doi.org/10.1002/cne.903600203.

Cardona, A., Saalfeld, S., Preibisch, S., Schmid, B., Cheng, A., Pulokas, J., Tomancak, P., and Hartenstein, V. (2010). An integrated micro- and macroarchitectural analysis of the Drosophila brain by computer-assisted serial section electron microscopy. PLoS Biol. *8*, e1000502. https://doi.org/10.1371/journal.pbio.1000502.

Chen, P., and Hong, W. (2018). Neural circuit mechanisms of social behavior. Neuron *98*, 16–30. https://doi.org/10.1016/j.neuron.2018.02.026.

Chen, P.B., Hu, R.K., Wu, Y.E., Pan, L., Huang, S., Micevych, P.E., and Hong, W. (2019). Sexually dimorphic control of parenting behavior by the medial amygdala. Cell *176*, 1206–1221.e18. https://doi.org/10.1016/j.cell.2019.01.024.

Chen, A.-X., Yan, J.-J., Zhang, W., Wang, L., Yu, Z.-X., Ding, X.-J., Wang, D.-Y., Zhang, M., Zhang, Y.-L., Song, N., et al. (2020). Specific hypothalamic neurons required for sensing conspecific male cues relevant to inter-male aggression. Neuron *108*, 763–774.e6. https://doi.org/10.1016/j.neuron.2020.08.025.

Choi, G.B., Dong, H.W., Murphy, A.J., Valenzuela, D.M., Yancopoulos, G.D., Swanson, L.W., and Anderson, D.J. (2005). Lhx6 delineates a pathway mediating innate reproductive behaviors from the amygdala to the hypothalamus. Neuron *46*, 647–660. https://doi.org/10.1016/j.neuron.2005.04.011.

Deisseroth, K. (2015). Optogenetics: 10 years of microbial opsins in neuroscience. Nat. Neurosci. *18*, 1213–1225. https://doi.org/10.1038/nn.4091.

Edelstein, A.D., Tsuchida, M.A., Amodaj, N., Pinkard, H., Vale, R.D., and Stuurman, N. (2014). Advanced methods of microscope control using μManager software. J. Biol. Methods *1*, 10. https://doi.org/10.14440/jbm.2014.36.

Franklin, K.B.J., and Paxinos, G. (2013). Paxinos and Franklin's the Mouse Brain in Stereotaxic Coordinates (Academic Press).

Gunaydin, L.A., Yizhar, O., Berndt, A., Sohal, V.S., Deisseroth, K., and Hegemann, P. (2010). Ultrafast optogenetic control. Nat. Neurosci. *13*, 387–392. https://doi.org/10.1038/nn.2495.

Haller, J. (2018). The role of central and medial amygdala in normal and abnormal aggression: a review of classical approaches. Neurosci. Biobehav. Rev. *85*, 34–43. https://doi.org/10.1016/j.neubiorev.2017.09.017.

Hashikawa, K., Hashikawa, Y., Falkner, A., and Lin, D. (2016). The neural circuits of mating and fighting in male mice. Curr. Opin. Neurobiol. *38*, 27–37. https://doi.org/10.1016/j.conb.2016.01.006.

Herman, A.M., Huang, L., Murphey, D.K., Garcia, I., and Arenkiel, B.R. (2014). Cell type-specific and time-dependent light exposure contribute to silencing in neurons expressing Channelrhodopsin-2. Elife *3*, e01481. https://doi.org/10.7554/eLife.01481.

Hong, W., Kim, D.W., and Anderson, D.J. (2014). Antagonistic control of social versus repetitive self-grooming behaviors by separable amygdala neuronal subsets. Cell *158*, 1348–1361. https://doi.org/10.1016/j.cell.2014.07.049.

Jun, N.Y., and Cardin, J.A. (2020). Activation of distinct channelrhodopsin variants engages different patterns of network activity. ENeuro *7*, ENEURO.0222-18.2019. https://doi.org/10.1523/ENEURO.0222-18.2019.

Keshavarzi, S., Sullivan, R.K.P., Ianno, D.J., and Sah, P. (2014). Functional properties and projections of neurons in the medial amygdala. J. Neurosci. *34*, 8699–8715. https://doi.org/10.1523/JNEUROSCI.1176-14.2014.

Kipp, M. (2001). Anvil - a generic annotation tool for multimodal dialogue. In Eurospeech-2001 (ISCA Archive), pp. 1367–1370.

Klapoetke, N.C., Murata, Y., Kim, S.S., Pulver, S.R., Birdsey-Benson, A., Cho, Y.K., Morimoto, T.K., Chuong, A.S., Carpenter, E.J., Tian, Z., et al. (2014). Independent optical excitation of distinct neural populations. Nat. Methods *11*, 338–346. https://doi.org/10.1038/nmeth.2836.

Lee, H., Kim, D.W., Remedios, R., Anthony, T.E., Chang, A., Madisen, L., Zeng, H., and Anderson, D.J. (2014). Scalable control of mounting and attack by Esr1+ neurons in the ventromedial hypothalamus. Nature *509*, 627–632. https://doi.org/10.1038/nature13169.

Lin, J.Y., Lin, M.Z., Steinbach, P., and Tsien, R.Y. (2009). Characterization of engineered channelrhodopsin variants with improved properties and kinetics. Biophys. J. *96*, 1803–1814. https://doi.org/10.1016/j.bpj.2008.11.034.

Lin, D., Boyle, M.P., Dollar, P., Lee, H., Lein, E.S., Perona, P., and Anderson, D.J. (2011). Functional identification of an aggression locus in the mouse hypothalamus. Nature *470*, 221–226. https://doi.org/10.1038/nature09736.

Lischinsky, J.E., and Lin, D. (2020). Neural mechanisms of aggression across species. Nat. Neurosci. *23*, 1317–1328. https://doi.org/10.1038/s41593-020-00715-2.

Lo, L., Yao, S., Kim, D.-W., Cetin, A., Harris, J., Zeng, H., Anderson, D.J., and Weissbourd, B. (2019). Connectional architecture of a mouse hypothalamic circuit node controlling social behavior. Proc. Natl. Acad. Sci. U S A *116*, 7503–7512. https://doi.org/10.1073/pnas.1817503116.

Madisen, L., Zwingman, T.A., Sunkin, S.M., Oh, S.W., Zariwala, H.A., Gu, H., Ng, L.L., Palmiter, R.D., Hawrylycz, M.J., Jones, A.R., et al. (2010). A robust and high-throughput Cre reporting and characterization system for the whole mouse brain. Nat. Neurosci. *13*, 133–140. https://doi.org/10.1038/nn.2467.

Mathis, A., Mamidanna, P., Cury, K.M., Abe, T., Murthy, V.N., Mathis, M.W., and Bethge, M. (2018). DeepLabCut: markerless pose estimation of user-defined body parts with deep learning. Nat. Neurosci. *21*, 1281–1289. https://doi.org/10.1038/s41593-018-0209-y.

Mattis, J., Tye, K.M., Ferenczi, E.A., Ramakrishnan, C., O'Shea, D.J., Prakash, R., Gunaydin, L.A., Hyun, M., Fenno, L.E., Gradinaru, V., et al. (2012). Principles for applying optogenetic tools derived from direct comparative analysis of microbial opsins. Nat. Methods *9*, 159–172. https://doi.org/10.1038/nmeth.1808.

Miczek, K.A., Brykczynski, T., and Grossman, S.P. (1974). Differential effects of lesions in the amygdala, periamygdaloid cortex, and stria terminalis on aggressive behaviors in rats. J. Comp. Physiol. Psychol. *87*, 760–771. https://doi.org/10.1037/h0036971.

Miller, S.M., Marcotulli, D., Shen, A., and Zweifel, L.S. (2019). Divergent medial amygdala projections regulate approach–avoidance conflict behavior. Nat. Neurosci. *22*, 565–575. https://doi.org/10.1038/s41593-019-0337-z.

Nagel, G., Ollig, D., Fuhrmann, M., Kateriya, S., Musti, A.M., Bamberg, E., and Hegemann, P. (2002). Channelrhodopsin-1: a light-gated proton channel in green algae. Science *296*, 2395–2398. https://doi.org/10.1126/science.1072068.

Nagel, G., Szellas, T., Huhn, W., Kateriya, S., Adeishvili, N., Berthold, P., Ollig, D., Hegemann, P., and Bamberg, E. (2003). Channelrhodopsin-2, a directly light-gated cation-selective membrane channel. Proc. Natl. Acad. Sci. U S A *100*, 13940–13945. https://doi.org/10.1073/pnas.1936192100.

Nagel, G., Brauner, M., Liewald, J.F., Adeishvili, N., Bamberg, E., and Gottschalk, A. (2005). Light activation of channelrhodopsin-2 in excitable cells of Caenorhabditis elegans triggers rapid behavioral responses. Curr. Biol. *15*, 2279–2284. https://doi.org/10.1016/j.cub.2005.11.032.

Nath, T., Mathis, A., Chen, A.C., Patel, A., Bethge, M., and Mathis, M.W. (2019). Using DeepLabCut for 3D markerless pose estimation across species and behaviors. Nat. Protoc. *14*, 2152–2176. https://doi.org/10.1038/s41596-019-0176-0.

Nilsson, S.R., Goodwin, N.L., Choong, J.J., Hwang, S., Wright, H.R., Norville, Z.C., Tong, X., Lin, D., Bentzley, B.S., Eshel, N., et al. (2020). Simple behavioral analysis (SimBA) – an open source toolkit for computer classification of complex social behaviors in experimental animals. Preprint at bioRxiv. https://doi.org/10.1101/2020.04.19.049452.

Nordman, J.C., and Li, Z. (2020). The dorsal raphe regulates the duration of attack through the medial orbitofrontal cortex and medial amygdala. eNeuro *7*, ENEURO.0331-20.2020. https://doi.org/10.1523/ENEURO.0331-20.2020.

Padilla, S.L., Qiu, J., Soden, M.E., Sanz, E., Nestor, C.C., Barker, F.D., Quintana, A., Zweifel, L.S., Ronnekleiv, O.K., Kelly, M.J., and Palmiter, R.D. (2016). Agouti-related peptide neural circuits mediate adaptive behaviors in the starved state. Nat. Neurosci. *19*, 734–741. https://doi.org/10.1038/nn.4274.

Raam, T., and Hong, W. (2021). Organization of neural circuits underlying social behavior: a consideration of the medial amygdala. Curr. Opin. Neurobiol. *68*, 124–136. https://doi.org/10.1016/j.conb.2021.02.008.

Schindelin, J., Arganda-Carreras, I., Frise, E., Kaynig, V., Longair, M., Pietzsch, T., Preibisch, S., Rueden, C., Saalfeld, S., Schmid, B., et al. (2012). Fiji: an open-source platform for biological-image analysis. Nat. Methods *9*, 676–682. https://doi.org/10.1038/nmeth.2019.

Schnütgen, F., Doerflinger, N., Calleja, C., Wendling, O., Chambon, P., and Ghyselinck, N.B. (2003). A directional strategy for monitoring Cre-mediated recombination at the cellular level in the mouse. Nat. Biotechnol. *21*, 562–565. https://doi.org/10.1038/nbt811.

Sineshchekov, O.A., Jung, K.-H., and Spudich, J.L. (2002). Two rhodopsins mediate phototaxis to low- and high-intensity light in Chlamydomonas reinhardtii. Proc. Natl. Acad. Sci. U S A *99*, 8689–8694. https://doi.org/10.1073/pnas.122243399.

Sparta, D.R., Stamatakis, A.M., Phillips, J.L., Hovelso, N., van Zessen, R., and Stuber, G.D. (2012). Construction of implantable optical fibers for long-term optogenetic manipulation of neural circuits. Nat. Protoc. *7*, 12–23. https://doi.org/10.1038/nprot.2011.413.

Stagkourakis, S., Spigolon, G., Williams, P., Protzmann, J., Fisone, G., and Broberger, C. (2018). A neural network for intermale aggression to establish social hierarchy. Nat. Neurosci. *21*, 834–842. https://doi.org/10.1038/s41593-018-0153-x.

Tang, W., Kochubey, O., Kintscher, M., and Schneggenburger, R. (2020). A VTA to basal amygdala dopamine projection contributes to signal salient

somatosensory events during fear learning. J. Neurosci. *40*, 3969–3980. https://doi.org/10.1523/JNEUROSCI.1796-19.2020.

Ting, J.T., Daigle, T.L., Chen, Q., and Feng, G. (2014). Acute brain slice methods for adult and aging animals: application of targeted patch clamp analysis and optogenetics. Methods Mol. Biol. *1183*, 221–242. https://doi.org/10.1007/978-1-4939-1096-0_14.

Tye, K.M., and Deisseroth, K. (2012). Optogenetic investigation of neural circuits underlying brain disease in animal models. Nat. Rev. Neurosci. *13*, 251–266. https://doi.org/10.1038/nrn3171.

Unger, E.K., Burke, K.J., Jr., Yang, C.F., Bender, K.J., Fuller, P.M., and Shah, N.M. (2015). Medial amygdalar aromatase neurons regulate aggression in both sexes. Cell Rep. *10*, 453–462. https://doi.org/10.1016/j.celrep.2014.12.040.

Vochteloo, J.D., and Koolhaas, J.M. (1987). Medial amygdala lesions in male rats reduce aggressive behavior: interference with experience. Physiol. Behav. *41*, 99–102. https://doi.org/10.1016/0031-9384(87)90137-5.

Vong, L., Ye, C., Yang, Z., Choi, B., Chua, S., Jr., and Lowell, B.B. (2011). Leptin action on GABAergic neurons prevents obesity and reduces inhibitory tone to POMC neurons. Neuron *71*, 142–154. https://doi.org/10.1016/j.neuron.2011.05.028.

Watakabe, A., Ohtsuka, M., Kinoshita, M., Takaji, M., Isa, K., Mizukami, H., Ozawa, K., Isa, T., and Yamamori, T. (2015). Comparative analyses of adeno-associated viral vector serotypes 1, 2, 5, 8 and 9 in marmoset, mouse and macaque cerebral cortex. Neurosci. Res. *93*, 144–157. https://doi.org/10.1016/j.neures.2014.09.002.

Wu, Y.E., Pan, L., Zuo, Y., Li, X., and Hong, W. (2017). Detecting activated cell populations using single-cell RNA-seq. Neuron *96*, 313–329.e6. https://doi.org/10.1016/j.neuron.2017.09.026.

Zhang, F., Aravanis, A.M., Adamantidis, A., de Lecea, L., and Deisseroth, K. (2007). Circuit-breakers: optical technologies for probing neural signals and systems. Nat. Rev. Neurosci. *8*, 577–581. https://doi.org/10.1038/nrn2192.

STAR★METHODS

KEY RESOURCES TABLE

REAGENT or RESOURCE	SOURCE	IDENTIFIER
Antibodies		
Chicken polyclonal anti-GFP	Abcam	Cat# ab13970; RRID:AB_300798
Rabbit polyclonal anti-RFP	Abcam	Cat# ab62341; RRID:AB_945213
Goat anti-chicken IgG Alexa Fluor 488 conjugated	Thermo Fisher Scientific	Cat# A-11039; RRID:AB_2534096
Donkey anti-rabbit IgG Alexa Fluor 568 conjugated	Thermo Fisher Scientific	Cat# A10042; RRID:AB_2534017
Deposited data		
Raw data	This study	https://doi.org/10.5281/zenodo.4311847
Experimental models: Organisms/strains		
Mouse: STOCK Slc32a1$^{tm2(cre)Lowl}$/J	Jackson Labs	RRID:IMSR_JAX:016962
Mouse: B6.Cg-Gt(ROSA)26Sor$^{tm9(CAG-tdTomato)Hze}$/J	Jackson Labs	RRID:IMSR_JAX:007909
Mouse: BALB/cByJ	Charles River	RRID:IMSR_JAX:001026
Recombinant DNA		
AAV8:hSyn:DIO:ChETA-eYFP	This study	Coding sequence identical to Addgene plasmid 26968
AAV8:hSyn:DIO:eGFP	This study	Coding sequence identical to Addgene plasmid 50457
AAV2:EF1α:DIO:ChR2-eYFP	University of North Carolina Vector Core, Chapel Hill, NC, USA	In-stock vector (Dr. Karl Deisseroth)
AAV2:EF1α:DIO:eYFP	University of North Carolina Vector Core	In-stock vector (Dr. Karl Deisseroth)
AAV2:EF1α:DIO:ChETA-eYFP	University of North Carolina Vector Core	In-stock vector (Dr. Karl Deisseroth)
AAV8:EF1α:DIO:ChR2-eYFP	University of Zürich Viral Vector Facility, Zürich, Switzerland	Cat# v214-8
AAV1:EF1α:DIO:ChETA-eYFP	University of Pennsylvania Vector Core, Philadelphia, PA, USA	Cat# AV-1-26968P; available from Addgene, Cat# 26968-AAV1
AAV8:CAG:DIO:tdTomato	University of North Carolina Vector Core	In-stock vector (Dr. Ed Boyden)
AAV8:EF1α:DIO:mCherry	University of Zürich Viral Vector Facility	Cat# v114-8
AAV2:EF1α:DIO:ChR2-mCherry	University of Zürich Viral Vector Facility	Cat# v80-2
Software and algorithms		
Acquisition software: EthoVisionXT	Noldus Information Technologies	https://www.noldus.com/ethovision-xt; RRID:SCR_000441
Video annotation tool: Anvil	Kipp (2001)	https://www.anvil-software.org/
Image analysis software: FIJI	Schindelin et al. (2012)	https://imagej.net/Fiji; RRID:SCR_002285
Image alignment tool: TrackEM2	Cardona et al. (2010)	https://imagej.net/TrakEM2
Data analysis and graphing software: IgorPro	WaveMetrics Inc.	https://www.wavemetrics.com/; RRID:SCR_000325
Pose estimation software: DeepLabCut v2.1.10	Mathis et al. (2018); Nath et al. (2019)	https://github.com/DeepLabCut/DeepLabCut
Automated classification of social behavior: SimBA v1.2	Nilsson et al. (2020)	https://github.com/sgoldenlab/simba; RRID:SCR_021413
Image acquisition software: Micro-Manager	Edelstein et al. (2014)	https://micro-manager.org/; RRID:SCR_016865
Electrophysiology acquisition: PatchMaster	HEKA Elektronik	https://www.heka.com/; RRID:SCR_000034
Statistical data analysis: Prism9	GraphPad	https://www.graphpad.com/; RRID:SCR_000306
Optic fiber/light cone reconstruction tool for IgorPro	This study	https://doi.org/10.5281/zenodo.4311847

(*Continued on next page*)

Continued

REAGENT or RESOURCE	SOURCE	IDENTIFIER
Other		
Optic fiber for the optogenetic fiber implants	Thorlabs	Cat# FT200UMT
Stereotaxic instrument for mice	David Kopf Instruments	Model 942 Small Animal Stereotaxic Instrument
473 nm DPSS laser	Changchun New Industries Optoelectronics	Cat# MBL-FN-473-150mW
1 × 2 fiber optic rotary joint	Doric Lenses	Cat# FRJ_1x2i_FC-2FC_0.22
TTL pulse generator	A.M.P.I.	Master-8
Slide scanning microscope	Olympus	VS120-L100
Confocal microscope	Carl Zeiss	LSM 700
Vibratome slicer	Leica Microsystems	VT1000S
Upright microscope for slice electrophysiology	Olympus	BX50WI
Patch-clamp amplifier	HEKA Elektronik	EPC-10
Temperature controlling system	Warner Instruments	Cat# TC-344B; Cat# PM-1; Cat# SHM-6
LED driver	Mightex Systems	Cat# BLS-SA02-US

RESOURCE AVAILABILITY

Lead contact

- Requests for information on reagents and resources as well as sharing requests should be directed to the Lead Contact, Dr. Olexiy Kochubey (olexiy.kochubey@epfl.ch).

Materials availability

- This study did not generate new unique reagents.

Data and code availability

- The data generated during this study have been deposited at the Zenodo repository and are publicly available as of the date of publication. The DOI is listed in the Key resources table.
- Original code has been deposited at Zenodo repository and is publicly available as of the date of publication. The DOI is listed in the Key resources table.
- Any additional information required to reanalyze the data reported in this paper is available from the lead contact upon request.

EXPERIMENTAL MODEL AND SUBJECT DETAILS

All procedures with laboratory mice (*mus musculus*) were authorized by the Service of Consumption and Veterinary Affairs (SCAV), Canton of Vaud, Switzerland (authorizations VD2885.0 and VD2885.1). We used the VGAT^{Cre} mouse line, which is a VGAT-internal ribosome entry site (IRES)-Cre line (STOCK Slc32a1$^{tm2(cre)Lowl}$/J; RRID:IMSR_JAX:016962, first described in Vong et al., 2011). In some experiments (Figure 1), we used VGAT^{Cre} × tdTomato mice, which were the offspring of a cross between VGAT^{Cre} line and a Cre-dependent tdTomato reporter mice Ai9 (B6.Cg-Gt(ROSA)26Sor$^{tm9(CAG-tdTomato)Hze}$/J; RRID:IMSR_JAX:007909, described in Madisen et al., 2010). VGAT^{Cre} mice were back-crossed to the C57Bl6/J line (RRID:IMSR_JAX:000664) for 2–4 generations; the tdTomato line was maintained on C57Bl6/J background. Healthy adult, virgin male mice were used in the resident-intruder aggression tests. A maximum of five mice were group-housed in cages containing enrichment materials (nesting material, plastic shelter, wooden bars, and a cardboard tunnel), at the specific pathogen free (SPF) animal facility of EPFL under a 12/12 h light/dark cycle, with food and water ad libitum. One day before surgery, the animals were separated into single cages. BALB/cByJ male mice (RRID:IMSR JAX:001026) were purchased from Charles River (Écully, France) and were group-housed until used as intruder mice in the resident-intruder test.

METHOD DETAILS

Viral vectors

To target channelrhodopsin and/or fluorophore expression to MeApd GABA neurons for *in-vivo* and *ex-vivo* experiments, we used Cre-recombinase dependent (FLEX/DIO; Schnütgen et al., 2003) adeno-associated viral vectors (AAV) of the serotypes 2/8, 2/2 and 2/1

(referred to as AAV8, AAV2, AAV1; see Key resources table). We used two modifications of the original wildtype channelrhodopsin-2 (Boyden et al., 2005; Nagel et al., 2003): a speed-optimized channelrhodopsin-$2^{H134R,E123T}$ ("ChETA"; Gunaydin et al., 2010), and an enhanced channelrhodopsin-2^{H134R} ("ChR2"; Nagel et al., 2005). For the production of the AAV8:hSyn:DIO:ChETA-eYFP and AAV8:hSyn:DIO:eGFP vectors used for our initial experiments (Figure 1), the DNA plasmids were derived from the plasmids pAAV:EF1α:DIO:ChETA-eYFP (plasmid #26968; Addgene, Watertown, MA, USA) and pAAV:EF1α:DIO:eYFP (Addgene plasmid #27056), respectively, by custom cloning and verified by sequencing. These two AAV8 vectors were packaged by the lab of Dr. Bernard Schneider (EPFL).

The previously used custom-made AAV2:EF1α:DIO:ChR2-2A-hrGFP vector (Hong et al., 2014) expressing channelrhodopsin-2^{H134R} (ChR2) was not publicly available. Therefore, we purchased a vector driving the Cre-dependent expression of ChR2 (AAV2:EF1α:DIO:ChR2-eYFP; see Key resources table). Indeed, with this vector, and with AAV8:EF1α:DIO:ChR2-eYFP, we were able to reproduce the previously reported stimulatory effect on aggression (see Figure 3). DNA sequence alignment confirmed that all the channelrhodopsin-encoding vectors used in our study had the sequences downstream of promoters identical to plasmids pAAV:EF1α:DIO:ChETA-eYFP (Addgene #26968) or pAAV:EF1α:DIO:ChR2-eYFP (Addgene #20298), originally donated by the lab of Dr. Karl Deisseroth. Other viral vectors were purchased from various suppliers (see Key resources table).

Stereotactic surgery procedures

$VGAT^{Cre}$ male mice (8–10 weeks old) in cohorts of 5–6 animals were randomly assigned to a test or to a control group. They were stereotaxically injected in the MeApd with an AAV vector encoding for a channelrhodopsin-fluorophore fusion construct (test group) or fluorophore only (control group). All procedures were identical between the control - and the test groups. Stereotaxic surgeries were made using a model 942 small animal digital stereotaxic instrument (David Kopf Instruments, Tujunga, CA, USA) under continuous gas anesthesia (1–1.5% isoflurane in O_2) with pre-operative local analgesia (a mix of bupivacaine and lidocaine injected subcutaneously). For additional analgesia, paracetamol was provided in the drinking water (1 mg/mL) starting one day before, and ending five days after surgery. For *in-vivo* optogenetic stimulation experiments (Figures 1 and 3), 200 nl of virus suspension was injected on each brain side into the MeApd with a pulled glass capillary at the following coordinates (in mm from bregma skull surface): ML ±2.3, AP -1.7, DV -5.3. Optic fiber implants were custom made of 200 μm core/0.39 NA optic fiber (FT200UMT; Thorlabs Inc, Newton, NJ, USA; implant transmission >70% at 473 nm as described by Sparta et al., 2012; see also Tang et al., 2020). During the surgery, the implants were vertically advanced to 500 μm above the virus injection sites and secured to the skull with a dental cement cup (Jet denture repair package; Cat#1234FIB; Lang Dental, Wheeling, IL, USA), and an anchoring screw (Cat#AMS90/1B-100; Antrin Miniature Specialties, Fallbrook, CA, USA). For *ex-vivo* patch-clamp recordings (Figures 4 and S4), the injected suspension (200 nL) consisted of a 1:1 mix of two viral vectors as indicated, and no optic fibers were implanted. For histological analysis of AAV2 and AAV8 vector tropism (Figures S3A–S3I), 100 nL of a 1:1 mix of the indicated viral vectors was injected into the left MeApd. For the analysis of a possible differential expression of ChETA and ChR2 (Figures S3J–S3P), 200 nL of an equimolar mix of the indicated viral vectors (diluted to the final titer of 2.36×10^{12} mL^{-1} for each vector), was bilaterally injected into the MeApd.

Behavioral testing

Following the surgery, the mice were housed individually. Four weeks after surgery, a resident-intruder test was performed under optogenetic stimulation. The testing was performed at the beginning of the dark cycle in the home cages of the operated mice under minimal ambient light levels. No change of bedding was made for a week before testing; enrichment materials (see above) were removed for the duration of the behavioral test. There was no pre-selection of animals based on their basal aggression or hierarchy rank. Prior to the resident-intruder test, the operated $VGAT^{Cre}$ resident mice were habituated to handling (being held in experimenter's hands, constraining and optic fiber patch cord attachment). Furthermore, the mice were habituated to the head tethering imposed by the optic fiber patch cords while exploring the home cage, during 4–5 daily sessions 15 min long each. The resident-intruder experiment consisted of a 5 min period when the resident animal was free to explore its home cage alone, followed by the introduction of an unfamiliar BALB/cByJ male intruder (8–9 weeks old) for the next ~25 min. After an initial period of interaction (~300 s), regularly spaced trains of light pulses were applied via the optic fiber patch cords of the resident mice (see e.g. Figures 1C, 1I, 3B, 3H, 3I, and 3L). Each mouse underwent two sessions of resident-intruder testing on subsequent days using different intruders; each intruder animal was used maximally twice. The behavior was continuously recorded with two synchronized CMOS cameras (acA1300-60gc; Basler AG, Ahrensburg, Germany) providing top- and side views, equipped with infrared long-pass filters and under infrared light illumination, at 30 fps under control of EthoVision XT 13 software (Noldus Information Technologies, Wageningen, The Netherlands). The same software recorded a TTL signal from a Master-8 stimulator (A.M.P.I., Jerusalem, Israel) representing the gate for the trains of blue light pulses. The blue light pulses were produced by a 473 nm diode pumped solid state laser (MBL-FN-473-150mW, Changchun New Industries Optoelectronics, Changchun, China) triggered with TTL pulse trains from the Master-8 stimulator, and directed toward the optic fiber implants through 200 μm core/0.22 NA optic patch cords (FC connector to 1.25 mm ferrule; Doric Lenses, QC, Canada) attached to a 1 × 2 intensity dividing fiber optic rotary joint (Doric Lenses). For each mouse, the laser power was adjusted to 10 mW at the tip of the optic fiber implant; in some experiments we adjusted to other light power levels (Figure S1). Light stimuli were 5 ms long, repeated at 20 Hz. We used a regular pattern of light trains (30–60 s long) interleaved with dark periods of fixed length (60 s), to avoid possible experimental bias. Such a bias could arise if the experimenter would trigger the light train manually during a short aggression bout, which could result in a stop of aggression apparently co-inciding with the stimulation by light.

Histology

For the post-hoc validation of channelrhodopsin expression and optic fiber placement above the MeApd (Figures 2 and S2), the animals were deeply anesthetized with intraperitoneal injection of pentobarbital, and transcardially perfused with 4% paraformaldehyde in phosphate buffered saline (PBS). After 24h post-fixation in 4% PFA and dehydration in 30% sucrose in PBS, 40 μm thick coronal brain sections were cut using a freezing sliding microtome (Hyrax S30; Carl Zeiss, Oberkochen, Germany).

For analyzing the distribution of AAV2- and AAV8-infected GABA neurons in the MeApd, a mix of AAV2:EF1α:DIO:eYFP and AAV8:CAG:FLEX:tdTomato, or a mix of AAV2:EF1α:DIO:eYFP and AAV8:EF1α:FLEX:mCherry viral vectors were used (Figures S3A–S3I). The animals were sacrificed 3 or 4 weeks after injection, respectively. For analyzing the co-expression of ChETA-eYFP and ChR2-mCherry, a mix of AAV2:EF1α:DIO:ChETA-eYFP and AAV2:EF1α:DIO:ChR2-mCherry viral vectors was used (Figures S3J–S3P). The animals were sacrificed 3 weeks after injection. Transcardial perfusion and coronal sections of the MeA were prepared as described above. For both types of experiments (Figure S3), immunohistochemistry was performed using 1:1000 diluted chicken anti-GFP (ab13970; Abcam, Cambridge, United Kingdom; RRID:AB_300798) and 1:500 rabbit anti-RFP antibodies (ab62341; Abcam; RRID:AB_945213) to stain against eYFP and tdTomato or mCherry, respectively. As the secondary antibodies, goat anti-chicken Alexa 488 (A11039; Thermo Fisher Scientific, Waltham, MA, USA; RRID:AB_2534096) and donkey anti-rabbit Alexa 568 antibodies (A10042; Thermo Fisher Scientific; RRID:AB_2534017) were used at 1:200 dilution.

In all cases, free-floating brain sections were mounted on glass slides and embedded in DAPI containing mounting medium (Fluoroshield™ with DAPI; F6057-20ML; Merck/Sigma-Aldrich, Darmstadt, Germany).

Image acquisition

Brain sections for post-hoc validation of fiber placements (Figures 2 and S2) were imaged with a slide scanning microscope (VS120-L100; Olympus, Tokyo, Japan) employing a 10x/0.4 NA objective. To analyze the distribution of AAV2- and AAV8-transduced neurons as well as ChR2-mCherry and ChETA-eYFP expressing neurons (Figure S3), tile images of up to 5 focal planes were acquired using an inverted confocal microscope (LSM 700; Carl Zeiss) equipped with a motorized stage, a 40x/1.3 NA oil objective (Figures S3A–S3C and S3J–S3L), or with a 20x/0.8 NA air objective (Figures S3D–S3I), and 405, 488 and 555 nm laser lines for exciting DAPI, YFP and tdTomato/mCherry, respectively. Image acquisition was done at the Bioimaging and Optics Platform (BIOP), EPFL.

Patch-clamp electrophysiology

A mouse at a time was sacrificed by decapitation after a brief anesthesia with 3% isoflurane in O_2 (according to authorized procedures; see above), and 300 μm thick coronal brain slices containing the MeApd were made using a Leica VT1000S vibratome (Leica Microsystems, Wetzlar, Germany). The experiments were performed 4–5 weeks following injection of the respective virus mix into the MeApd (Figure 4). Brain slices were prepared with an N-methyl-D-glutamine (NMDG) based solution containing (in mM): 110 NMDG, 2.5 KCl, 1.2 NaH_2PO_4, 25 $NaHCO_3$, 20 HEPES, 25 D-glucose, 5 sodium ascorbate, 2 thiourea, 3 sodium pyruvate, 10 $MgCl_2$, 0.5 $CaCl_2$ (pH 7.3; Ting et al., 2014). The slices were then kept in a holding solution containing (in mM): 92 NaCl, 1.2 NaH_2PO_4, 30 $NaHCO_3$, 20 HEPES, 25 D-glucose, 5 sodium ascorbate, 3 thiourea, 3 sodium pyruvate, 2 $MgCl_2$, 2 $CaCl_2$ (pH 7.3). Whole-cell patch clamp recordings were performed using an extracellular solution containing (in mM): 124 NaCl, 2.5 KCl, 1.2 NaH_2PO_4, 30 $NaHCO_3$, 20 HEPES, 10 D-glucose, 5 sodium ascorbate, 2 thiourea, 3 sodium pyruvate, 2 $MgCl_2$, 2 $CaCl_2$ (pH 7.4, continuously bubbled with 95% O_2/5% CO_2). Recording pipettes were made from borosilicate glass (Hilgenberg, Germany) and had resistances of 3–5 MOhm when filled with a pipette solution containing (in mM): 8 KCl, 145 K-gluconate, 10 HEPES, 3 Na-phosphocreatine, 4 Mg-ATP, 0.3 Na-GTP, 5 EGTA; pH 7.26, with KOH; 315 mosm). Slices were visualized with an upright BX50WI microscope (Olympus) equipped with a 60x/0.9 NA water-immersion objective (LUMPlanFI, Olympus), and whole-cell patch-clamp recordings were done with an EPC-10 patch-clamp amplifier under the control of PatchMaster software (HEKA Elektronik, Reutlingen, Germany). The temperature of the extracellular solution in the recording chamber was maintained at 34–36°C using a PM-1 heated platform, an SHM-6 inline solution heater and a TC-344B controller (Warner Instruments, Holliston, MA, USA). Series resistances (R_s) were 17.2 ± 0.9 and 17.9 ± 1.4 MOhm (for ChETA and ChR2 recordings; n = 35 and n = 31; p = 0.99, Mann-Whitney test) and were not compensated electronically. Brain slices were illuminated with a Dodt-type infrared gradient contrast and imaged using a CMOS camera (C11440-52U; Hamamatsu Photonics, Hamamatsu City, Japan) under control of MicroManager software (Edelstein et al., 2014). To visualize the eYFP or tdTomato/mCherry fluorescence, the fluorophores were excited using custom-fitted high-power LEDs (CREE XP-E2 Royal blue, 465 nm, and Green, 535 nm, respectively; Cree Inc, Durham, NC, USA) under control of a BioLED driver (BLS-SA02-US; Mightex Systems, Toronto, Canada), and imaged using appropriate dichroic mirrors and emission filters. Short pulses (5 ms) of a blue LED at maximal power (~80 mW/mm^2 at the focal plane with 60x objective) were used for exciting ChETA or ChR2. oIPSCs were measured with 1s long trains of blue light stimuli (5 ms length, repetition rate of 20 Hz); the holding potential was 0 mV, close to the reversal potential of the ChR2-or ChETA mediated currents.

QUANTIFICATION AND STATISTICAL ANALYSIS

Analysis of behavior data

The behavioral data was initially manually scored using the Anvil video annotation tool (https://www.anvil-software.org/; Kipp, 2001). During analysis, the scorer was blind to the timing of the optogenetic light train. During manual scoring, each video frame was

exclusively classified as one of 23 elementary behaviors of the resident mouse: 1) attack; 2) tail rattle; 3) catching with paws; 4) proactive approach; 5) sniffing/touching the intruder's body; 6) sniffing the body while following the intruder; 7) mouse/nose sniffing; 8) anogenital sniffing; 9) anogenital sniffing while following; 10) tail sniffing; 11) licking the intruder; 12) mounting the intruder; 13) being sniffed by intruder; 14) being followed; 15) being attacked; 16) being licked; 17) escaping from intruder; 18) grooming; 19) digging; 20) moving at a distance from the intruder; 21) resting at a distance; 22) rearing; 23) active avoidance. Display and averaging of the resulting behavioral traces was done using custom routines in IgorPro 7.08 (WaveMetrics, Lake Oswego, OR, USA). We combined the traces of elementary behaviors (see above) into the following six groups using a logical "OR": "aggression" (behaviors #1–3), "following" (#6, 8–9), "social contact" (#4, 5, 7, 10, 11), "asocial" (#18, 19, 22, 23), "passive" (#13–17) and "resting/moving" (#20, 21). Note that mounting (#12) was not included in any of these groups because we have virtually never observed spontaneous nor light-evoked mounting in these experiments. The resulting six behavior traces were aligned to the onsets of the blue light trains and averaged across repeated trains for a given mouse (see e.g. Figures 1E and 1G). To quantify the effect of blue light exposure, we compared the relative time of aggressive behavior during the first 30 s of the light train, to the last 30 s of the preceding dark period (see e.g. Figure 1E). The results of this analysis were averaged for each animal between two subsequent days of resident-intruder testing, yielding one final data point per animal in the summary plots (e.g. Figure 1H).

About one-third of the behavioral experiments performed toward the end of the study was analyzed from the top-view videos using an automated procedure according to DeepLabCut - SimBA behavior classification framework (Nilsson et al., 2020). For body part tracking we used DeepLabCut v2.1.10 (Mathis et al., 2018; Nath et al., 2019). In total, 882 frames from 5 videos (binned to 640 × 350px; 95%/5% train/test ratio) were manually annotated for 8 body points per animal (the nose tip, the ears, the body center, the body sides, the tail base and the tail tip; Nilsson et al., 2020). A deep convolutional neural network ResNet-50 was trained in DeepLabCut with default parameters on a Google Colab platform (https://colab.research.google.com) for 600000 iterations (train error 1.99, test error 12.44 px with p-cutoff 0.9; shuffle 1), and the resulting snapshot was used to predict trajectories of the body points for each of the two mice. The trajectories were processed in SimBA v1.2 (Nilsson et al., 2020), where the random forest classifiers for six grouped behaviors were trained on a manually annotated dataset based on six videos (total ~153 min), comprising the following total frames per behavior: 10518 ("aggression"), 3880 ("following"), 43279 ("social contact"), 18923 ("asocial"), 13267 ("passive"), 186263 ("resting/moving"). Behavioral predictions by SimBA were further analyzed in IgorPro. Validation of the SimBA predictions on a set of 33 manually annotated test videos revealed 97.9 ± 0.5% accuracy, 61.3 ± 5.8% positive predictive value (precision), 54.3 ± 3.9% false negative (miss) rate, 99.3 ± 0.2% true negative rate (specificity) for the aggressive behavior.

Analysis of illuminated brain areas

The slide scanner images of brain sections for post-hoc validation of fiber placement were manually aligned into a serial stack using FIJI TrackEM2 (Cardona et al., 2010; Schindelin et al., 2012). A custom tool in IgorPro (see Key resources table) was used for navigation through the stack and for fitting a model of the optic fiber into the fiber track visible on the images, in order to calculate the 3D location of an idealized light cone emanating from the fiber, thereby taking into account the fiber tilt. For computing a cone-shaped volume illuminated by light, we used the core diameter and numerical aperture of the fiber, and assumed a 500 μm limit for the light propagation in brain tissue (Aravanis et al., 2007). The contours of a brain atlas (Franklin and Paxinos, 2013) were overlaid onto the images using Adobe Illustrator (Adobe Inc, Mountain View, CA, USA). Finally, the areas of the relevant brain nuclei, their overlap with the extent of the channelrhodopsin expression, and the percentage overlap with the light cone were quantified in IgorPro. The respective areas were summed across the serial brain sections to approximate the fractions of volume (see Figures 2B, 2C, S2B, and S2C).

Analysis of expression patterns in the MeA

To analyze the distribution of AAV2- and AAV8-transduced neurons (Figures S3A–S3I), non-overlapping ROIs were manually drawn using FIJI on confocal tile images around each neuron expressing eYFP or tdTomato/mCherry, and the mean intensities and centroid coordinates of these ROIs were imported into IgorPro for analysis. The cells were classified as either expressing, or non-expressing the fluorescent reporter protein when the mean ROI fluorescence intensity exceeded a threshold of 150% and 200% of the mean background fluorescence value in the whole MeApd for the red and the green channels, respectively. Based on this classification, binary maps of reporter (co-) expression by individual cells were generated (Figures S3D, S3F and S3H). For the analysis of the expression of ChR2 and ChETA across MeApd GABA-neurons (Figures S3J–S3P), the cells were manually classified into ChR2-mCherry positive, ChETA-eYFP positive, or ChETA/ChR2 co-expressing cells based on their fluorescent signal. ROIs were drawn around the cells in FIJI to mark their spatial positions used for generating the binary maps (Figure S3M).

Electrophysiological data analysis

Electrophysiological recording data were imported into IgorPro for analysis using custom routines. Peak amplitudes of light-gated channelrhodopsin currents and of oIPSCs (Figures 4C–4F) were measured at −70 mV and 0 mV holding potential, respectively, in response to the first light pulse in a train (Figures 4A and 4B; the second from top, and the bottom panels, respectively). For some cells, the first light pulse evoked an unclampable Na^+-current; in those cases, the value of the light-gated current was readout at the point of the falling slope change (if apparent; see Figure 4B inset), or as the peak of the next well-clamped channelrhodopsin-mediated current. The ChR2 or ChETA-evoked plateau potential during the 20 Hz/5 ms light trains, was quantified as the average

voltage offset over resting V_m, after low-pass filtering <10 Hz to remove the action potential (AP) transients. Deactivation time constants of the two channelrhodopsin variants (see Results) were estimated by single-exponential fits to the decay of light-gated currents upon the last pulse in a train. Synaptic charge transfer (Figure 4G) was estimated by integrating the oIPSC trace over 1 s long train of light pulses (Figures 4A and 4B, bottom panels) after the baseline current subtraction; cells with the negative integral values due to negligible IPSC amplitudes were excluded. Analysis of the APs during the 30s trains of light pulses (Figures 4H–4J) was limited to cells expressing a direct current of >60 pA, which led to exclusion of n = 2 and n = 4 cells from the ChR2 and ChETA groups, reducing the sample to n = 25 and 18 recordings, respectively. For the absolute AP peak amplitude measurements during 30 s light trains (Figures 4H and 4I), fast voltage transients time-locked to the light pulses were classified as APs if they exceeded a 20 mV threshold relative to the passive membrane response level; the latter was estimated by filtering the voltage trace <10 Hz in a procedure identical to the determination of the plateau potential (see above). Only the cells that displayed no failures during the indicated time periods were admitted for analysis in Figure 4I; note that the cell numbers contributing to the average traces dropped faster for ChR2 than for ChETA, respectively, due to the AP-failures in ChR2 expressing cells. To quantify the number of successful APs generated during optogenetic trains (Figure 4J), APs were detected based on an arbitrary threshold of 0 mV (see dashed line in Figure 4H) and considered as a failure if the AP peak amplitude dropped below this value during the train.

Classification of the cells into intrinsic AP firing types (Figure S4C) was performed manually by an observer, based on the cell membrane voltage response to step current injections (from −100 to +320 pA in 30 pA increments relative to the holding current; Figure S4C). For this, the passive and active (AP firing dynamics) membrane properties were analyzed with custom routines in IgorPro to extract information on the time course of AP frequency during the current step depolarizations, and on the maximal firing frequency as a function of injected current (Figure S4C). Passive membrane properties such as the input resistance and membrane time constant were also documented, as well as the presence of a negative voltage sag (quantified as a "sag ratio"). The following definitions of the firing types were then used for classification (see Figure S4C for examples). Type 1: Neurons that respond with only a single AP to depolarizing current steps, then the AP firing cease. Type 2: Neurons that slowly adapt to a low spiking frequency at small injected currents, and that generate only a short burst of APs upon intermediate to large current steps. Type 3: Neurons generating a brief high-frequency burst of APs which then rapidly adapts to a low (<50 Hz) steady-state frequency. Type 4: Neurons showing no clear adaptation of the AP firing frequency, and in some cases augmentation of instantaneous AP frequency with a maximum between the second and the third APs. Type 5: High-frequency spiking neurons slowly adapting to a relatively high steady-state AP frequency (≥50 Hz) at intermediate injected currents, and expressing no negative voltage sag. Type 6: Neurons with AP firing dynamics as for the type 5 neurons, but expressing a negative voltage sag (a signature of I_h current, in some cases leading to post-hyperpolarization rebound AP). Note that at the largest amplitudes of the depolarizing current steps, some type 5 and 6 neurons ceased to fire APs after a short period of AP frequency adaptation (Figure S4C).

Statistical data analysis

No prior sample size calculation was performed. Resident-intruder experiments with optogenetic modulation were usually performed in small cohorts at a time of n = 3 and n = 3 mice for the test group (expressing ChETA or ChR2) and for the control group (expressing eYFP or eGFP); experiments were repeated with several cohorts for each condition. Statistical tests were performed using GraphPad Prism 9 (GraphPad Software, USA). A Shapiro-Wilk test for normality was used to determine if the data was normally distributed before choosing a parametric or non-parametric test type. In case of two-sample datasets, either a paired or two-sample t test, or Wilcoxon or Mann-Whitney U tests were performed as indicated in the Results (Figures 1, 3, 4C–4G, S1, S3, and S4). To compare the timecourses of AP amplitudes (Figure 4I; n = 20 data points per cell in each time range), two-way repeated-measures ANOVA (RM-ANOVA) was performed for each time range to analyze effects of the channelrhodopsin variant and of the time, followed by Holm-Šidák's multiple comparison test. For the analysis of AP following (Figure 4J), the average firing frequency was calculated in two 15s bins for each group, and a two-way RM-ANOVA analysis was performed followed by Šidák's multiple comparison test. To compare the fractional proportions of cells expressing different channelrhodopsin constructs (Figure S3P), we pooled the cells counted across several sections from the same animal (n = 4 mice), and performed a nested one-way ANOVA test followed by Tukey's multiple comparison test. The test types and resulting significance levels are reported in the Results text and indicated in the figures by star symbols according to: $p < 0.05$, *; $p < 0.01$, **; $p < 0.001$, ***; n.s., non-significant.

Cell Reports, Volume *39*

Supplemental information

Stimulation of medial amygdala GABA neurons with kinetically different channelrhodopsins yields opposite behavioral outcomes

Aiste Baleisyte, Ralf Schneggenburger, and Olexiy Kochubey

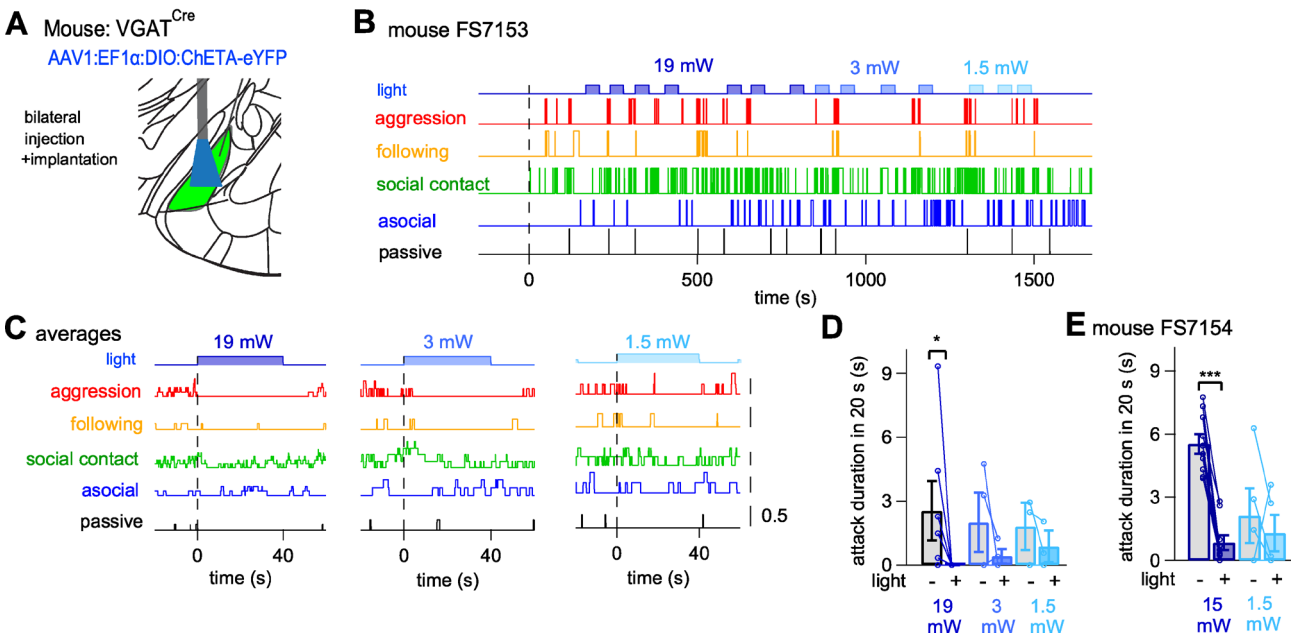

Figure S1. The inhibition of aggression by optogenetic activation of MeApd GABA neurons with ChETA depends on light power. Related to Figure 1.

(A) Schematic of the approach for virus injection and optic fiber placement in the MeApd. In these experiments, an AAV1 vector (AAV1:EF1α:DIO:ChETA-eYFP) was used to express ChETA.

(B) Behavior quantified during a resident-intruder test with a ChETA-expressing mouse. Trains of light pulses (5 ms at 20 Hz rate, 473 nm) were applied for 40s at varying light intensities as indicated (19 mW, 3 mW and 1.5 mW; color-coded).

(C) Average behavior traces aligned to the onset of the light trains (B) of the indicated intensities. Note the interruption of ongoing aggression at higher light intensities (19 or 3 mW), whereas less intense trains (1.5 mW) did not have an apparent effect.

(D, E) Quantification of the time spent attacking immediately before ("light -") and during ("light +") the optogenetic stimulation trains delivered at different light intensities. Data for the same mouse as shown in B-C (D), and for another mouse (E) is shown. Significant differences were observed at 19 mW ($p = 0.031$, $n = 7$ trains in D), and 15 mW ($p = 0.001$, $n = 10$ trains in E; one-tailed Wilcoxon matched-pairs signed rank test). Data are represented as mean ± SEM.

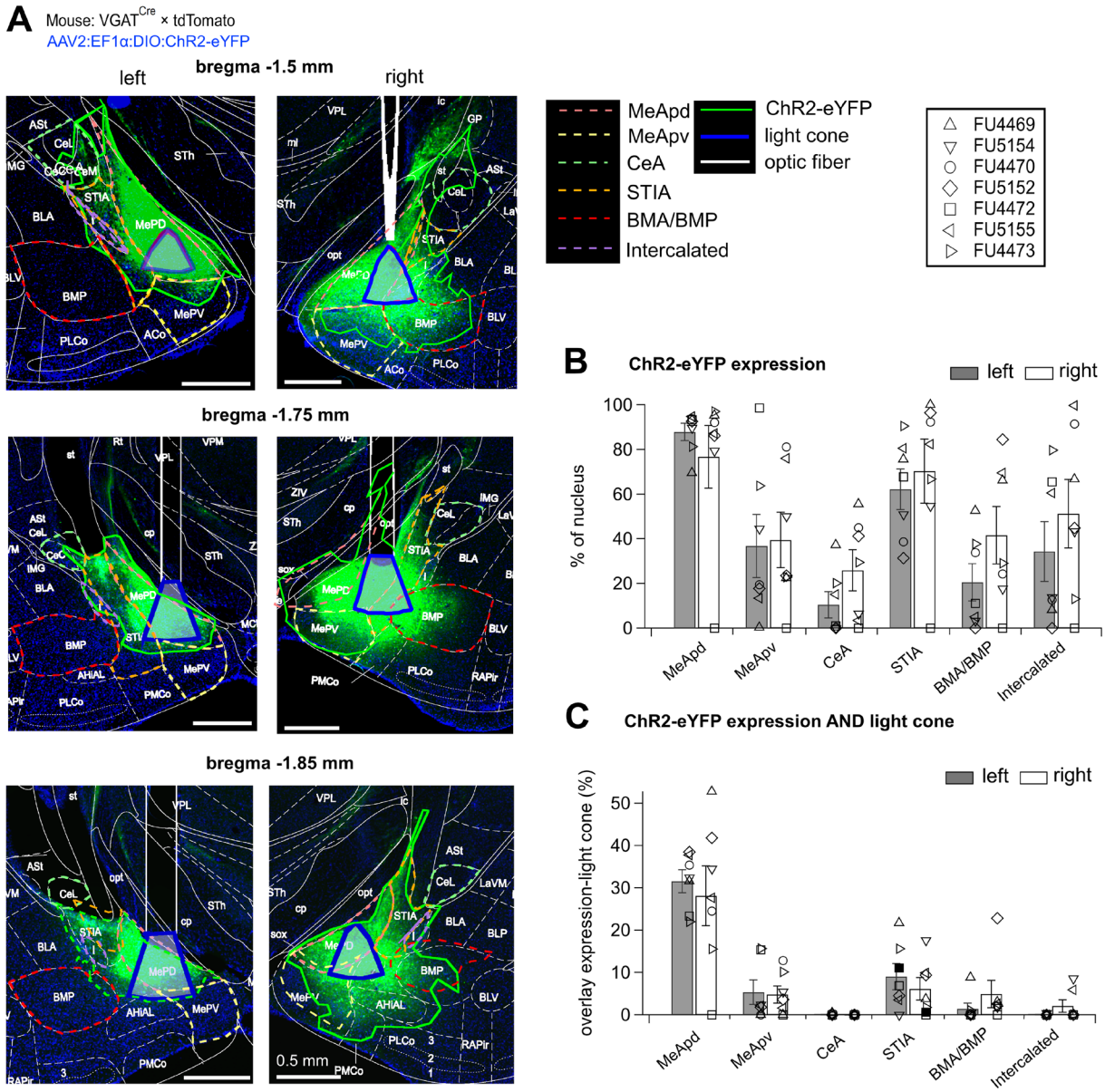

Figure S2. Histological analysis to identify the brain areas targeted by optogenetic stimulation with ChR2 expressed using AAV2 vector. Related to Figure 3.

We performed a quantitative post-hoc histological analysis, analogous to that in Figure 2, but for a cohort of n = 7 VGAT^{Cre} mice injected with AAV2:EF1α:DIO:ChR2-eYFP, that gave rise to the behavior data in Figures 3A-D, 3G-H. The results (B, C) are very similar to those shown in Figures 2B, 2C for a cohort of VGAT^{Cre} mice expressing ChETA under AAV8 vector. They indicate that mainly the MeApd was targeted for optogenetic stimulation with ChR2. We thus conclude that there were no detectable differences in the targeted expression of the channelrhodopsin-variant, nor in the optic fiber placement, between the optogenetic stimulation experiments using ChETA (Figure 1) and ChR2 (Figure 3A-D, 3G-H). Data are represented as mean ± SEM.

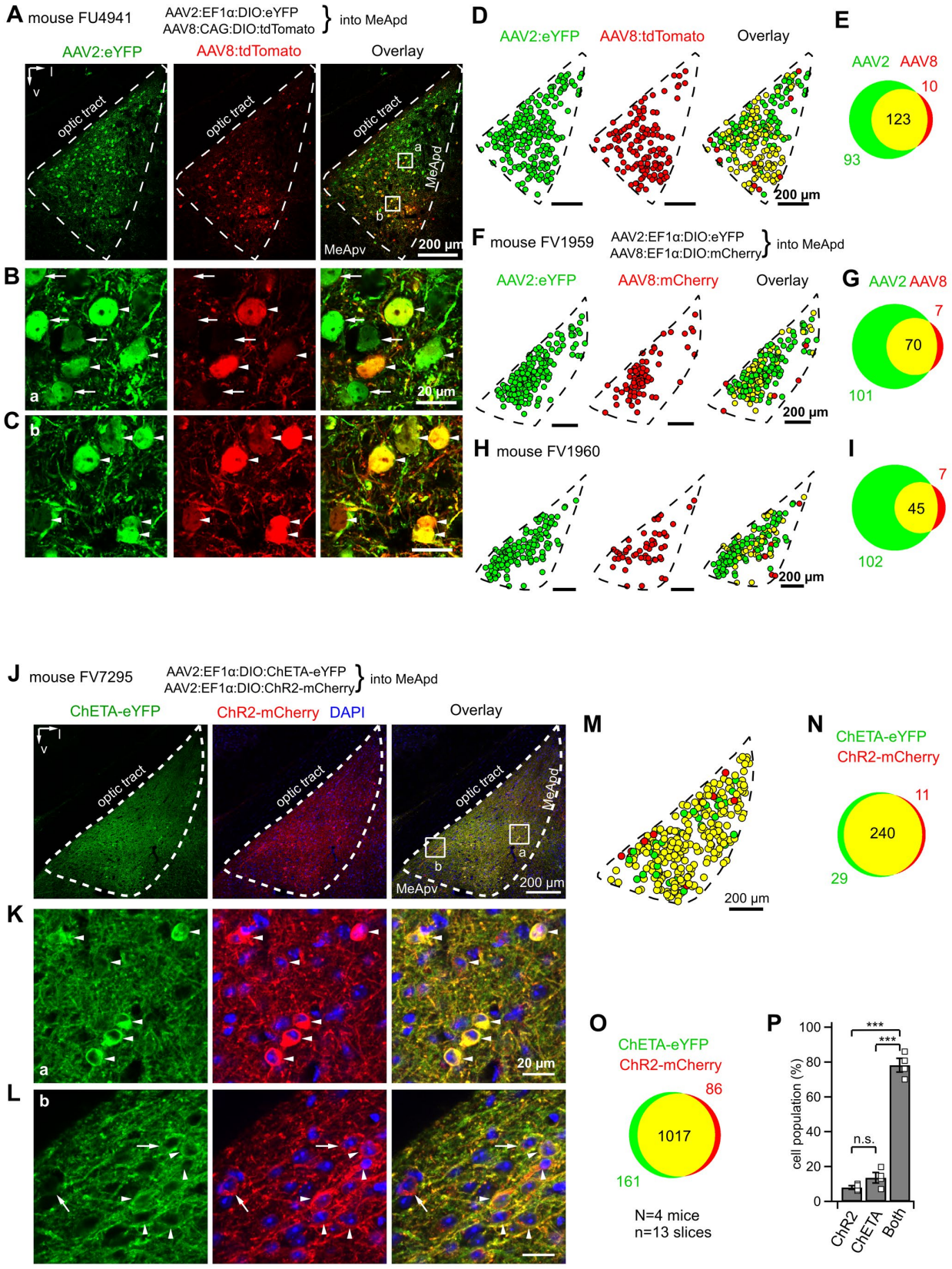
A mouse FU4941
AAV2:EF1α:DIO:eYFP
AAV8:CAG:DIO:tdTomato
into MeApd
AAV2:eYFP
AAV8:tdTomato
Overlay
optic tract
MeApd
MeApv
200 µm
B
C
20 µm
D
E
AAV2 AAV8
10
123
93
F mouse FV1959
AAV2:EF1α:DIO:eYFP
AAV8:EF1α:DIO:mCherry
into MeApd
AAV8:mCherry
G
7
70
101
H mouse FV1960
I
7
45
102
J mouse FV7295
AAV2:EF1α:DIO:ChETA-eYFP
AAV2:EF1α:DIO:ChR2-mCherry
into MeApd
ChETA-eYFP
ChR2-mCherry
DAPI
K
L
M
N
11
240
29
O
86
1017
161
N=4 mice
n=13 slices
P
cell population (%)
n.s.
***
ChR2
ChETA
Both

Figure S3. Analysis of expression overlap in MeApd GABA neurons after transduction with AAV2 and - 8 vectors, and co-expression of ChR2 and ChETA. Related to Figure 3.

(A) Overview confocal images of a coronal brain section containing the MeApd (dashed outline), obtained from a $VGAT^{Cre}$ mouse after injection with a mix of viral vectors AAV2:EF1α:DIO:eYFP (green channel; eYFP) and AAV8:CAG:DIO:tdTomato (red channel; tdTomato). Final titers of the injected vectors in a mix were $2.25 \cdot 10^{12}$ and $3.25 \cdot 10^{12}$ ml^{-1}, respectively.
(B, C) High-magnification images of the areas marked with white rectangles in (A). *Arrows* point out example neurons expressing *only* eYFP from the AAV2 vector (green channel); *arrowheads* point out neurons expressing tdTomato from an AAV8 serotype vector (red channel). The tdTomato-positive neurons often co-expressed eYFP (overlay, appearing yellow).
(D) Binary maps showing the identity and location of neurons in (A) that express either a single marker (green or red), or both fluorescent proteins (yellow).
(E) A Venn diagram showing the number of neurons transduced by the AAV2 vector alone (green), by the AAV8 vector alone (red), or by both vectors (yellow) in the same mouse as in (A-D). For the Venn diagram, n = 2 confocal sections were analyzed.
(F - I) Localization maps and Venn diagrams as in (D, E), but obtained from another two $VGAT^{Cre}$ mice four weeks after co-injection with AAV2:DIO:eYFP and AAV8:DIO:mCherry (n = 5 sections were analyzed).
Altogether, the histological results in (A-I) show that AAV2 infected a larger number of MeApd GABA neurons than AAV8 (207 ± 19 %), and that only 7.5 ± 2.2 % of all transduced neurons were transduced by AAV8 alone (n = 7 sections from n = 3 mice). Thus, AAV8-transduced neurons are essentially a sub-population (~ half) of the AAV2-transduced neurons.
J) The experiments in panels J-P investigated whether ChR2 and ChETA are expressed in different sub-population of MeApd GABA neurons. The images in (J) show overview confocal images, obtained from a $VGAT^{Cre}$ mouse after injection with an equimolar mix of AAV2:EF1α:DIO:ChETA-eYFP (green channel) and AAV2:EF1α:DIO:ChR2-mCherry (red channel; DAPI signal is in blue). The final titers of the vectors were $2.36 \cdot 10^{12}$ ml^{-1} each. Fluorescence of the eYFP and mCherry reporters was enhanced with immunostaining (see STAR Methods).
K, L) High-magnification images of the areas marked with white rectangles in (J). *Arrows* point out example neurons expressing *only* ChETA-eYFP (green) or ChR2-mCherry (red). *Arrowheads* point to neurons expressing both ChETA-eYFP and ChR2-mCherry (yellow in overlay).
M) Binary map showing the identity and location of neurons expressing both variants (yellow), or ChR2-mCherry alone (red), or ChETA-eYFP alone (green), in the section shown in (J).

N) Venn diagram showing the number of neurons expressing ChETA-eYFP only (green, 10.4%), ChR2-mCherry only (red, 3.9%), or by both (yellow, 85.7%), counted in the example section (J, M) from one representative mouse.

O) Venn diagram showing the number of neurons expressing ChETA-eYFP, ChR2-mCherry or both constructs, pooled from n = 13 section from a total n = 4 mice.

P) Summary on the average fractions of cells expressing ChETA-eYFP or ChR2-mCherry or both constructs simultaneously, analyzed from n = 13 sections from n = 4 animals (see O for the total cell numbers). A nested one-way ANOVA ($p<10^{-4}$; $F_{2,36}=198.2$), followed by a Tukey´s multiple comparison test, showed a significantly higher fraction of cells expressing both ChETA-eYFP and ChR2-mCherry constructs (78.3 ± 3.9%; $p<10^{-4}$), while there was no statistical difference between the populations expressing only ChETA-eYFP or ChR2-mCherry (13.7 ± 3.0% or 8.1 ± 1.1%, respectively; p=0.289). Data are represented as mean ± SEM.

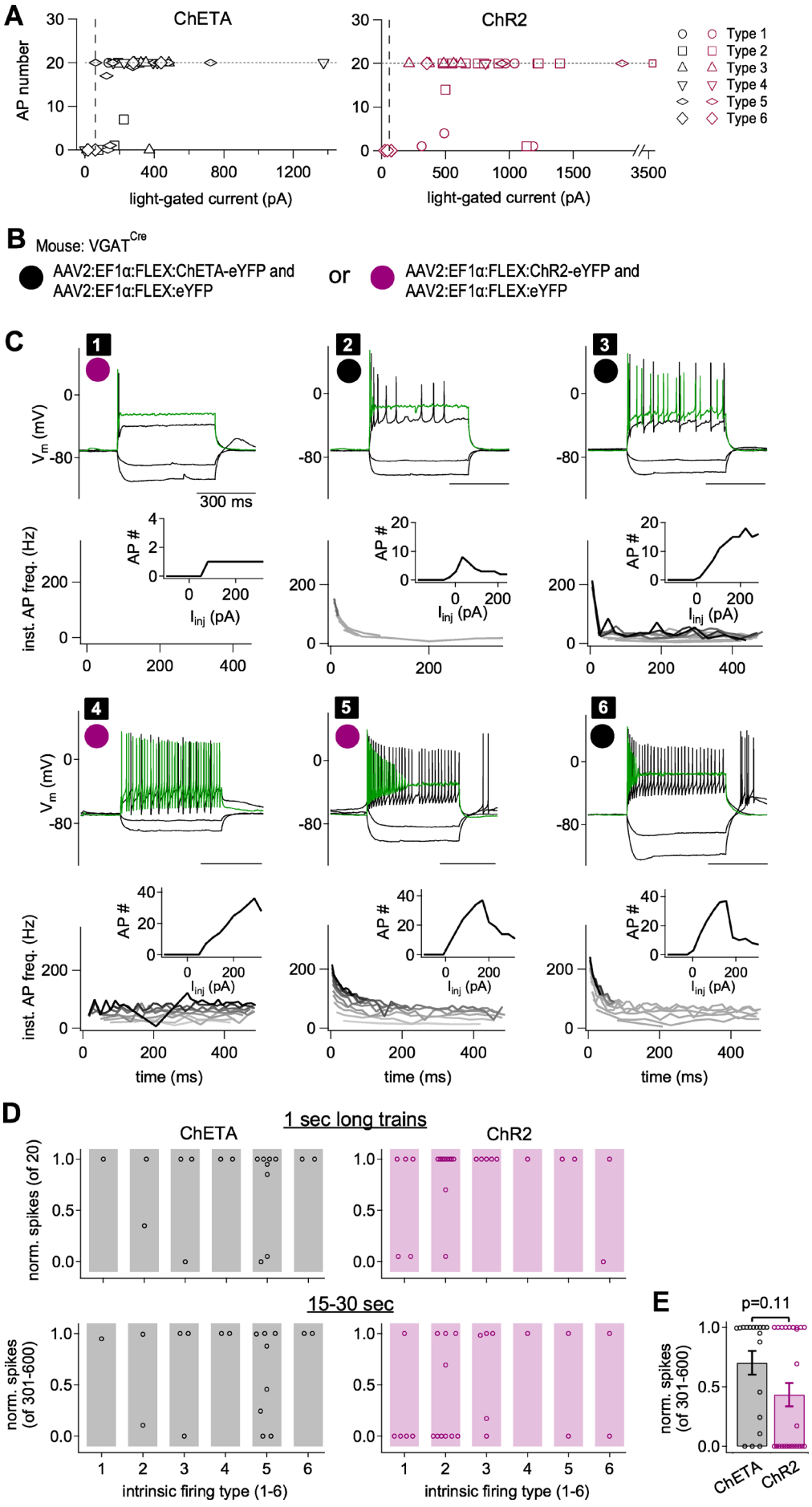
A
ChETA
ChR2
AP number
light-gated current (pA)
Type 1
Type 2
Type 3
Type 4
Type 5
Type 6
B
Mouse: VGAT^Cre
AAV2:EF1α:FLEX:ChETA-eYFP and AAV2:EF1α:FLEX:eYFP
or
AAV2:EF1α:FLEX:ChR2-eYFP and AAV2:EF1α:FLEX:eYFP
C
Vm (mV)
300 ms
inst. AP freq. (Hz)
AP #
Iinj (pA)
time (ms)
D
1 sec long trains
15-30 sec
norm. spikes (of 20)
norm. spikes (of 301-600)
intrinsic firing type (1-6)
E
p=0.11
norm. spikes (of 301-600)
ChETA
ChR2

Figure S4. AP firing types identified amongst MeApd GABA neurons, and distributions of optogenetically evoked AP-firing performance across the cell types. Related to Figure 4.

(A) AP-following performance of MeApd GABA neurons in response to 1s long 20 Hz light trains in the experiments shown in Figure 4A-G, under ChETA (left, n = 35) or ChR2 (right, n = 31). For each neuron, the number of APs generated in response to 20 light pulses is plotted as a function of the light-gated current amplitude. The vertical dashed line shows a current amplitude of 60 pA, below which neurons were not able to generate APs. The markers indicate the firing type classification of each neuron (as classified in C).

(B) Experimental approach to express either ChETA or ChR2 in MeApd GABA neurons, in combination with a soluble cytosolic eYFP marker for cell identification using a second co-injected AAV2 vector.

(C) Examples of membrane potential (V_m) responses of MeApd GABA neurons for each identified AP firing type (designated 1 to 6). The affiliation of each example recording to the ChETA or ChR2 group is indicated by black and magenta circles, respectively. The top panels show responses to current injections steps: two hyperpolarizing (-100 and -40 pA) and two depolarizing (+110 and +290 pA; the latter in green). The bottom panels show the time-course of instantaneous AP frequency (darker traces show responses to larger depolarizing current steps), and the total number of elicited APs as a function of injected current (insets). See STAR Methods for the criteria of classification into six AP-firing types.

(D) Top panels: normalized number of APs during 1s long 20 Hz trains, applied in the same recordings in which 30s trains were applied (Figure 4H-J), segregated according to the AP-firing type (as in C). Bottom panels: normalized number of APs during the second half of the 30s trains (see Figure 4J, 15-30s interval), segregated according to the AP-firing types. It can be seen that certain neurons that still followed the 1s trains, dropped out during the last 15s of the long trains. Furthermore, some neurons did not follow the trains well during the 1s trains. Nevertheless, the data set was too small (n = 18 and 25 for ChETA and ChR2) to arrive at statistically meaningful differences in AP-following stratified across the six different AP-firing types.

(E) Quantification of the data for the time interval of 15-30s of the long trains (D, bottom panels; Figure 4J), combined over all AP-firing types in each group ($p = 0.11$; Mann-Whitney test). Note that this comparison is the same as indicated in Figure 4J for the second half of the train. Data are represented as mean ± SEM.